Phase dynamics of patterns: The effect of boundary-induced amplitude variations

D. Roth,[1] M. Lücke,[1] M. Kamps,[2] and R. Schmitz[3]
[1]*Institut für Theoretische Physik, Universität des Saarlandes, 66041 Saarbrücken, Germany*
[2]*Höchstleistungsrechenzentrum, Forschungszentrum, 52425 Jülich, Germany*
[3]*Institut für Festkörperforschung, Forschungszentrum, 52425 Jülich, Germany*
(Received 17 May 1994)

A generalized phase diffusion equation is derived that incorporates spatial variations of the pattern amplitude. We investigate on the one hand the spatiotemporal relaxation behavior of initially prepared phase perturbations and on the other hand the structure and dynamics of damped phase waves that are forced by time-periodic, spatially localized perturbations. For the two paradigmatic cases of Rayleigh-Bénard convection (RBC) in the form of straight parallel rolls and of axisymmetric Taylor vortex flow (TVF), we compare the results of the phase equation for finite setups in quantitative detail with finite-difference numerical simulations of the full two-dimensional hydrodynamic field equations, with Ginzburg-Landau (GL) equations, and with various experiments. The phase equation can be transformed into a Schrödinger-like form with a potential that is determined by the amplitude variations. The free relaxation of phase perturbations is determined by a Sturm-Liouville eigenvalue problem, and the long-time behavior is governed by its lowest *positive* eigenvalue. This defines an effective diffusion constant D, which is considerably enhanced relative to the reference value D_0 in an ideal system with constant amplitude. Using the GL amplitude profiles one finds that D/D_0 depends only on a specific combination of driving control parameter and system length. Furthermore, one can apply supersymmetry commutation relations to relate the diffusive eigenvalues and eigenmodes of TVF and RBC to each other. For the latter case, the phase equation has a spatially homogeneous phase eigenmode with a zero eigenvalue that admits a free undamped pattern shift as a whole, while inhomogeneities of the phase relax away with higher diffusive eigenmodes. In the full system of equations there appears, instead of the zero-eigenvalue dynamics, a more complicated nondiffusive ultraslow phase dynamics that allows one to reanalyze recent phase diffusion experiments in RBC. Also, the spatially varying decay rates and wave numbers of periodically forced damped phase waves are shown to depend on amplitude variations and the finiteness of the system. We elucidate this dependence and show how these wave characteristics differ from each other and show that they are in general unrelated to the phase diffusion constant.

PACS number(s): 47.10.+g, 47.27.Te, 47.32.−y, 02.60.−x

I. INTRODUCTION

During the past decade or so the concept of characterizing certain structural and dynamical properties of patterns that arise in structure forming systems by their phase field has proved to be quite useful. This method is particularly fruitful to describe the spatiotemporal behavior and response of the pattern on long space and time scales [1,2]. The method was originally introduced in the context of periodic convective structures [3] and subsequently widely used [3–22], e.g., to investigate the stability of periodic patterns [3–9], wave number selection [4,6,10–13], defect dynamics [14], transition to turbulence [15], and other questions.

In this paper we elucidate the influence of boundary-induced amplitude variations of the structure on its phase dynamics. To that end, we derive a phase equation that is a generalized diffusion equation into which enters the amplitude of the pattern. This approach is rather general and applicable to various structures. We treat in explicit quantitative detail the two paradigmatic cases of Taylor vortex flow (TVF) and Rayleigh-Bénard convection (RBC) where the flow patterns are effectively one dimensional [2]. For both these systems we compare results of the phase equation with our extensive numerical simulations of the full hydrodynamic field equations, with numerical solutions of Ginzburg-Landau equations (GLE), and with experiments. We verify that the time scale separation of the slow long-time phase dynamics from the faster modulus dynamics leads to an effective decoupling of the former from the latter.

In such a situation our phase equation can be brought after a simple transformation into a Schrödinger-like form $\partial_t\psi=[\partial_x^2-V(x)]\psi$ with a potential term $V(x)$ that reflects the particular form of boundary-induced amplitude variations. The potential $V=(\partial_x^2 R)/R$ is determined by the curvature of the final-state modulus $R(x)$ of the flow amplitude. Thus, in the absence of modulus variations, $R=$const, one recovers a genuine diffusion equation. We use the generalized diffusion equation to investigate the influence of a spatially varying modulus, i.e., the influence of a nonzero potential $V(x)$ on (i) the free decay of initial phase perturbations and (ii) on the damped phase waves that are generated by a spatially localized time-periodic forcing of the phase.

Initial phase perturbations decay to zero with a spatiotemporal dynamics that is governed by the eigenvalues and eigenfunctions of the "Hamilton" operator

$H=-\partial_x^2+V(x)$. Its lowest *nonvanishing* eigenvalue describing the long-time phase relaxation determines an effective diffusion constant D. Thus, one immediately infers that D is enhanced (diminished) relative to the reference value D_0 in an ideal infinite system with $R=$const or $V=0$, when $R(x)$ is convex (concave)—a positive (negative) potential $V=(\partial_x^2 R)/R$ increases (decreases) the "ground-state energy" of H, i.e., the lowest eigenvalue that governs the long-time dynamics. Evaluating $R(x)$ and $V(x)$ with the GLE, one finds that the effective diffusion constant D depends only on one parameter, $\alpha=\sqrt{\epsilon}L/\xi_0$, which is a combination of control parameter ϵ, system length L, and correlation length ξ_0. In fact, plotting the TVF diffusion constants obtained in experiments [19,20] and in numerical simulations for different L and ϵ versus the parameter α, one finds almost universal behavior for the enhancement of D relative to D_0. This enhancement of diffusion by the end-wall-induced TVF amplitude variations is quite spectacular and, moreover, it is well explained by the phase theory with the modulus $R_{\mathrm{TVF}}(x)$ taken from the GLE.

The GLE moduli for RBC and TVF are given in terms of Jacobian elliptic functions such that

$$R_{\mathrm{RBC}}(x)=\mathrm{const}/R_{\mathrm{TVF}}(x)\ .$$

This causes a supersymmetry relation between the two "Hamiltonians"—since they are commutation partners, all their nonzero eigenvalues are the same.

In the RBC case with vanishing convective field amplitudes at the sidewalls, a zero eigenvalue appears. It implies that a spatially homogeneous phase perturbation does not decay—the pattern can be shifted uniformly within the phase equation approximation—while spatial inhomogeneities of the phase relax diffusively with a spatiotemporal dynamics described by higher diffusive modes and eigenvalues. The latter can be identified also in the numerical simulations of the full field equations on not-too-long time scales. After that, i.e., after spatial inhomogeneities have effectively decayed, the full field equations show a different nondiffusive ultraslow phase dynamics. The appearance of this motion instead of a free phase motion predicted by the zero eigenvalue of the GLE is influenced by an interaction between phase and sidewall that is not captured by the GLE. Its properties vary with L and ϵ separately. This analysis also shows us how to interpret the experimental data of Croquette and Schosseler [17].

In the last part of this paper we investigate within the framework of our phase equation phase waves that are generated by spatially localized low frequency periodic forcing. Local decay rates $\mathcal{K}_r(x)$, and local wave numbers $\mathcal{K}_i(x)$ of these waves are influenced by the finiteness of the system and in addition by spatial variations of the pattern amplitude. Recent experimental parameters and measurement locations [16,20] happened to be such that the measured $\mathcal{K}_r(x)$ and $\mathcal{K}_i(x)$ were close to the value $\mathcal{K}_0=\sqrt{\omega/(2D_0)}$. The latter results in a semi-infinite system within a genuine diffusion equation from a pure Stokes layer driven at frequency ω. In general, however, $\mathcal{K}_r$ and $\mathcal{K}_i$ deviate from each other and from $\mathcal{K}_0$ and, moreover, these two quantities are unrelated to phase diffusion. Furthermore, the properties of forced phase waves depend less sensitively on the spatial variations of the pattern amplitude than the long-time free diffusive relaxation of initial phase perturbations.

Our work is organized as follows: In Sec. II we describe the experimental setups to which our theory applies. Then we derive the phase equation and give an overview of the mathematical implications. In Sec. III we present solution methods for the Sturm-Liouville eigenvalue problem that arises when describing the free decay of initial phase perturbations. In Sec. IV we present amplitude profiles and potentials for RBC and TVF within the GLE approximation. We solve the phase equation and we determine effective diffusion constants. The results are compared with diffusion experiments and simulations in Sec. V. Section VI investigates forced phase waves and Sec. VII contains a conclusion.

II. LONG-TIME PHASE DYNAMICS

To introduce the reader to the problem and to illustrate the concepts, we briefly describe an idealized experiment which simplifies actual realizations [19,20]. Consider a Taylor-Couette (TC) apparatus of length L whose inner cylinder rotates with constant angular velocity, while the outer one stays at rest. The driving is above the critical value for the onset of Taylor vortices and the system is filled with a stationary vortex pattern. This pattern can be characterized by the strength and the position of each vortex. Let us now move one end plate inwards so carefully that the strength and the number of the vortices do not change. Obviously, the whole structure must shrink and the vortices must rearrange their position. Monitoring the location of an arbitrary vortex center, one finds that it relaxes roughly exponentially towards its final position. This gives the idea of treating the problem with a simple diffusion equation,

$$\partial_t\varphi(x,t)=D_0\partial_x^2\varphi(x,t) \tag{2.1}$$

for a phase

$$\varphi(x,t)=\phi(x,t)-\phi(x,t=\infty) \tag{2.2}$$

connected to the deviation of the vortices from their final configuration [21]. The variable x denotes the axial position. The solution of (2.1),

$$\varphi(x,t)=\sum_{n=1}^{\infty} a_n \sin\left[n\pi\frac{x}{L}\right]e^{-n^2\gamma_0 t}\ , \tag{2.3}$$

describes the relaxation towards the final phase profile $\phi(x,t=\infty)$. For long times the relaxation dynamics is governed by the lowest, $n=1$, spatial mode $\sin(\pi x/L)$, the amplitude of which relaxes with the rate

$$\gamma_0=\frac{\pi^2}{L^2}D_0\ . \tag{2.4}$$

However, comparing the above spatiotemporal relaxation behavior with that of experiments and numerical simulations of the full hydrodynamic field equations, one finds (cf. Sec. V A 1) that the boundary-induced spatial varia-

tion of the TVF pattern amplitude causes considerable changes. These boundary effects cannot be incorporated directly into (2.1) by imposing some suitable boundary condition on φ since by definition, and in view of the fact that the "gentle" relaxation behavior of φ does not change the number of vortices, φ has homogeneous boundary conditions at the two ends,

$$\varphi(x=0,t)=\varphi(x=L,t)=0 .$$

To derive an extension of (2.1), we use as a starting point the Ginzburg-Landau equation. This also gives us the opportunity of transferring the results to other systems, where a similar GLE is valid. Thus, one can regard the following theory as a general one, with TVF and RBC being special application examples. Furthermore, we want to emphasize that the resulting phase equation is structurally independent of the choice of the starting GLE; only the coefficients might change a little. This follows from the work of Kramer *et al.* [11]. A further advantage of using a GLE is the fact that all of its coefficients are known and mostly checked experimentally [22–30]. So, quantitative comparison with the phase dynamics observed in experiments and numerical simulations is possible.

The GLE for the complex amplitude,

$$A(x,t)=R(x,t)e^{i\phi(x,t)} , \tag{2.5a}$$

of a supercritically bifurcating one-dimensional pattern like RBC or TVF is [25,31,32]

$$\tau_0\partial_t A=(\epsilon+\xi_0^2\partial_x^2-g|A|^2)A \tag{2.5b}$$

or

$$\tau_0\partial_t R=[\epsilon+\xi_0^2\partial_x^2-\xi_0^2(\partial_x\phi)^2-gR^2]R , \tag{2.5c}$$

$$\tau_0 R\,\partial_t\phi=\xi_0^2[R\,\partial_x^2+2(\partial_x R)\partial_x]\phi , \tag{2.5d}$$

respectively. In the TC case, we use the relative deviation

$$\epsilon=\frac{\Omega}{\Omega_c}-1 \tag{2.5e}$$

of the rotation rate Ω of the inner cylinder from the critical value Ω_c for onset of TVF as control parameter. In the RB system,

$$\epsilon=\frac{\Delta T}{\Delta T_c}-1 \tag{2.5f}$$

is the relative deviation of the temperature difference between the hot bottom and the cold top of the fluid layer from the critical one, ΔT_c, for onset of RBC. For the TC systems with nonrotating outer cylinder that we shall investigate here, one has $\tau_0=0.037\,96d^2/\nu$ and $\xi_0=0.2694d$ when the radius ratio $\eta=r_1/r_2$ is 0.75. These values have been obtained by interpolating data of Ref. [24]. Here $d=r_2-r_1$ is the gap width and ν the kinematic viscosity of the fluid in the annulus. For the RB system on the other hand, $\tau_0=0.076\,93d^2/\kappa$ and $\xi_0=0.3848d$ if, e.g., the Prandtl number $\mathrm{Pr}=\nu/\kappa$ is 1 [24]. Here d is the height of the fluid layer and κ the thermal diffusivity.

The wave vector of the pattern lies in the x direction. The modulus relaxes to its final profile,

$$R(x)=R(x,t=\infty) , \tag{2.6}$$

on a typical time scale of τ_0/ϵ, while the phase reaches equilibrium on the scale $1/\gamma_0=L^2/(\pi^2 D_0)$ (2.4) on which, e.g., the vortices relax to their final positions. Here,

$$D_0=\xi_0^2/\tau_0 \tag{2.7}$$

is the phase diffusion constant for a reference system in which $A(x,t)$ reaches a final state A_0 with spatially constant modulus and phase, i.e., $D_0^{\mathrm{TVF}}=1.912\nu$ and $D_0^{\mathrm{RBC}}=1.924\kappa$.

We shall investigate here situations where the relaxation time of the modulus is much shorter than that of the phase:

$$\frac{\tau_0}{\epsilon}\ll\frac{1}{\gamma_0} , \tag{2.8a}$$

or equivalently

$$\alpha\gg\pi . \tag{2.8b}$$

Here we have introduced the quantity

$$\alpha=\sqrt{\epsilon}L/\xi_0 . \tag{2.9}$$

We found this combination [33] of system length and supercritical control parameter to characterize the long-time phase diffusion behavior of RBC and TVF (cf. following sections).

In systems that satisfy (2.8), the time scale separation causes an effective decoupling of the slow phase dynamics from the faster modulus dynamics. We thus formulate a decoupling approximation by using in the phase equation (2.5d) the final equilibrated modulus profile $R(x)$. This approximation leads to the phase equation

$$\left\{\frac{1}{D_0}R(x)\partial_t-2[\partial_x R(x)]\partial_x-R(x)\partial_x^2\right\}\varphi(x,t)=0 , \tag{2.10}$$

to be studied in this paper with $R(x)$ as input. For example, for an infinitely long system, $R(x)$ would be constant, reducing (2.10) to (2.1). The main deviation in (2.10) from the ordinary diffusion equation comes in standard finite setups from the boundaries at $x=0,L$ that cause the bulk homogeneous modulus profile to be deformed there. For example, for RBC one typically has $R=0$ at the end walls of convective channels [27,32]. Nonrotating rigid end plates in the TC setup, on the other hand, induce an increase of the TVF amplitude that grows with the inverse distance from the end [25,29,36]. We shall come back to the concrete forms of $R(x)$ in Sec. IV A.

We should like to stress that the quality of the decoupling approximation (2.10) for the phase equation is very good: Comparing numerical integrations of the full GLE (2.5b) for typical experimental parameters with results

from (2.10), we found no significant deviations in the long-time phase dynamics.

III. SOLUTION METHODS FOR THE STURM-LIOUVILLE EIGENVALUE PROBLEM OF THE PHASE EQUATION

Before determining the long-time phase dynamics for the concrete modulus profiles of RBC and TVF, we discuss here methods and some mathematical properties of the phase equation (2.10). It can be solved with a separation ansatz,

$$\varphi(x,t)=\varphi(x)e^{-\gamma t}\,, \tag{3.1}$$

where γ and $\varphi(x)$ are eigenvalues and eigenfunctions, respectively, of the Sturm-Liouville (SL) eigenvalue problem [37]

$$\mathcal{L}\varphi(x)=\left\{R(x)\partial_x^2+2[\partial_x R(x)]\partial_x+\lambda\frac{\pi^2}{L^2}R(x)\right\}\varphi(x)=0\,. \tag{3.2a}$$

Here we have introduced the reduced eigenvalue

$$\lambda=\gamma/\gamma_0\,, \tag{3.2b}$$

using the phase relaxation rate $\gamma_0=(\pi^2/L^2)D_0$ (2.4) and diffusion constant D_0 of a pattern with homogeneous amplitude A_0 as a reference. With the homogeneous boundary conditions $[a\varphi(0)+b\varphi'(0)]=0$ and $[c\varphi(L)+d\varphi'(L)]=0$, the operator $\mathcal{L}$ in (3.2a) is Hermitian with a real eigenvalue spectrum [37]. When $R(x)$ is positive everywhere as for TVF, the SL problem (3.2) is regular [37] and all eigenvalues λ_n are distinct and positive. For a singular situation like RBC with $R(x=0,L)=0$, a zero eigenvalue appears. The eigenfunctions $\hat{\varphi}_n(x)$ of (3.2) form a complete orthogonal function system. Hence the solution of the phase equation (2.10) can be expanded as

$$\varphi(x,t)=\sum_{n=1}^{\infty}a_n\hat{\varphi}_n(x)e^{-\gamma_n t}\,, \tag{3.3}$$

with $\gamma_n=\lambda_n\gamma_0$.

We define an effective diffusion constant D by the smallest, nonzero, positive eigenvalue of (3.2):

$$D/D_0=\min_{\lambda>0}\lambda_n=\gamma_{\min}/\gamma_0\,. \tag{3.4}$$

Its deviation from 1 reflects the effect of the boundary-induced spatial variation of $R(x)$ on the long-time phase relaxation. As an aside, we mention that within the GLE the relaxation to a final phase-winding amplitude, $A(x)=Re^{i\phi(x)}$ with homogeneous modulus and phase $\phi(x)=(k-k_c)x$, is described by a diffusion constant

$$D_0(k,\epsilon)=D_0\frac{\epsilon-3\xi_0^2(k-k_c)^2}{\epsilon-\xi_0^2(k-k_c)^2}\,, \tag{3.5}$$

where k_c is the critical wave number of the pattern. Here we shall investigate the effect of nonhomogeneous final-state *modulus profiles* $R(x)$ on phase diffusion. Because of the particular form of the boundary conditions to the phase variable (time independent and allowing self-adjointness), the final phase profile will be stationary. In Sec. VI we shall treat a situation with explicitly time-dependent boundary conditions.

A. Matrix representation and truncation approximations

Before we present in Sec. III B our method to determine and describe the phase dynamics, we briefly review for the sake of completeness in this subsection the results [22] of determining the eigenvalue spectrum of (3.2) algebraically.

1. The method

The method [22] transforms the differential equation (3.2) into a matrix equation:

$$(T_{nm}-\lambda S_{nm})\varphi_m=0\,, \tag{3.6}$$

by expanding into a suitable complete orthonormal function system:

$$\varphi(x)=\sum_{n=1}^{\infty}\varphi_n|n\rangle\,. \tag{3.7}$$

Then the differential operator $\mathcal{L}$ in (3.2) is represented by a matrix as in quantum mechanical problems from where the bra-ket notation is taken. The matrix elements are

$$S_{nm}=\langle n|R|m\rangle,\quad T_{nm}=-\frac{L^2}{\pi^2}\langle n|R\partial_x^2+2(\partial_x R)\partial_x|m\rangle\,. \tag{3.8}$$

To determine the lowest lying eigenvalues of (3.6) that control the long-time relaxation behavior of $\varphi(x,t)$, the matrices S and T are evaluated and truncated in successively increasing order.

2. Two analytically solvable test problems

We checked the numerical approximation scheme against two problems for which the eigenvalue spectrum can be given analytically with the method described in Sec. III B. The modulus profile

$$R(x)=e^{-x/l}+e^{-(L-x)/l} \tag{3.9a}$$

of our first test problem corresponds to a regular SL problem and looks for $l<L$ somewhat similar to that of TVF. Increasing towards the boundaries, this $R(x)$ is convex with a minimum at $x=L/2$. The resulting eigenvalues are

$$\lambda_n=n^2+\frac{1}{\pi^2}\frac{L^2}{l^2}\,, \tag{3.9b}$$

with $n=1,2,\ldots$. Hence the effective diffusion constant (3.4),

$$D=D_0\left[1+\frac{1}{\pi^2}\frac{L^2}{l^2}\right]\,, \tag{3.9c}$$

is larger than D_0. A physical explanation for this enhancement of the diffusion constant will be discussed in Sec. III B.

Our second test profile allowing an analytical determination of the eigenvalue spectrum is concave:

$$R(x)=\cos\left[\beta\pi\frac{x-L/2}{L}\right] . \tag{3.10a}$$

It displays for $\beta\leq 1$ some of the characteristics of the RBC modulus. It is maximal in the middle at $L/2$ and drops off towards the value $\cos(\beta\pi/2)$ at the ends. Hence for $\beta=1$, where $R(x=0,L)=0$, this problem becomes singular. The eigenvalues are

$$\lambda_n=n^2-\beta^2 . \tag{3.10b}$$

For the concave modulus profile (3.10a), the effective diffusion constant is reduced for $\beta<1$ to

$$D=D_0(1-\beta^2) . \tag{3.10c}$$

The lowest lying eigenvalue (3.10b), and with it the effective diffusion constant, decreases as the amplitude at the boundaries approaches zero. For the singular situation $R(x=0,L)=0$ with $\beta=1$, the smallest *nonvanishing* eigenvalue is $\lambda_2=3$, leading to $D=3D_0$.

3. *Expansion into sin(nπx/L)*

We found that for regular SL problems, for which $R(x)>0$ everywhere, the basis set

$$|n\rangle=\sqrt{2/L}\sin\left[n\pi\frac{x}{L}\right] \tag{3.11}$$

consisting of the eigenfunctions of (3.2) for the special case $R(x)=$const is well suited for the determination of the lowest eigenvalues. For a singular problem with $R(x=0,L)=0$, Legendre polynomials are preferable. They give rise to a faster convergence in the sequence of eigenvalue problems that arise with increasing truncation order of S and T (3.8). For the basis (3.11), one has [22]

$$\begin{aligned} S_{nm}&=R_{n-m}-R_{n+m} , \\ T_{nm}&=m(2n+m)R_{n+m}+m(2n-m)R_{n-m} , \end{aligned} \tag{3.12a}$$

$$R_j=\frac{1}{L}\int_0^L dx\cos\left[j\pi\frac{x}{L}\right]R(x) . \tag{3.12b}$$

Here already the lowest truncation at order 1 yields an approximation

$$D\simeq D_0\frac{R_0+3R_2}{R_0-R_2} \tag{3.13}$$

for the effective diffusion constant that is, at least for regular problems, quite close to the exact one and, moreover, gives physical insight [22].

B. Formulation as a Schrödinger equation

We introduce the function

$$\psi(x,t)=R(x)\varphi(x,t) , \tag{3.14a}$$

so that the phase equation (2.10) becomes

$$\left[\frac{1}{D_0}\partial_t-\partial_x^2+\frac{\partial_x^2 R}{R}\right]\psi(x,t)=0 . \tag{3.14b}$$

Here the curvature of the modulus plays the role of a potential

$$V(x)=\frac{\partial_x^2 R(x)}{R(x)} . \tag{3.15}$$

Its deviation from zero reflects the influence of the ends on the modulus. The separation ansatz (3.1)

$$\psi(x,t)=\psi(x)e^{-\gamma t} , \tag{3.16}$$

with $\psi(x)=R(x)\varphi(x)$, leads to the stationary Schrödinger equation (SSE)

$$\left[-\partial_x^2+V(x)-\lambda\frac{\pi^2}{L^2}\right]\psi(x)=0 , \tag{3.17a}$$

where

$$\lambda=\frac{\gamma}{\gamma_0}\quad\text{with}\quad\gamma_0=\frac{\pi^2}{L^2}D_0 \tag{3.17b}$$

as before. Again, the lowest lying eigenvalue ("energy") governs the long-time relaxation behavior of the ("wave") function $\psi(x,t)$ and is used to define an effective diffusion constant $D/D_0=\min_{\lambda>0}\lambda_n$. The dynamics here is relaxational in contrast to that of the time-dependent Schrödinger equation because the time derivative term in (3.14) is real. But all the knowledge and experience accumulated in quantum mechanics for the SSE may be taken over for (3.17).

Within the quantum mechanical picture, one can infer two important conclusions about the influence of a spatially varying modulus on the phase diffusion without further calculation. The "ground state energy," i.e., the smallest eigenvalue and with it the diffusion constant, increases relative to the reference case $V=0$, i.e., $R=$const, when finite size effects make the modulus R convex, i.e., when V becomes positive. Conversely, concave moduli, i.e., negative potentials V, decrease the "ground state energy" and hence the diffusion constant. Thus a convex modulus implies $D>D_0$, while a concave profile of R entails $D<D_0$. Of course, if the smallest eigenvalue is zero, the latter implication does not hold, because D is, by definition, determined by the smallest *nonvanishing* eigenvalue.

1. *Boundary conditions for ψ(x)*

We consider here only the two cases: (i) $R(x)$ is positive everywhere as for TVF and (ii) $R(x)$ vanishes only at the ends $x=0,L$ as for RBC. Case (i) with a nonzero modulus requires $\varphi=0$ at the ends, since with a fixed number of vortices in the system during the final stage of the relaxation, the phase does not change at the ends, i.e., $\phi(t)=\phi(t=\infty)$ at $x=0,L$. Hence, $\psi=R\varphi=0$ is the boundary condition for case (i). For case (ii) with a vanishing R at the ends, the phase $\phi(t)$ might change there. But $R=0$ implies $\psi=0$ unless the phase change φ

diverges which would imply the generation or creation of an infinite number of rolls. Hence in both cases the appropriate boundary condition is $\psi=0$ at the ends.

With this boundary condition the SSE describes in the quantum mechanical language a particle in a one-dimensional well with infinite potential walls at $x=0,L$ and a bottom shape given by $V(x)$. The infinite barriers at $x=0,L$ reflect the boundary conditions $\psi(x=0,L)=0$.

2. *Appearance and significance of a zero eigenvalue*

All modulus profiles $R_0(x)$ that vanish at both ends and are positive elsewhere give rise to a zero eigenvalue, $\lambda=0$, with eigenfunction $\psi_0(x)=R_0(x)$ and associated constant phase $\psi_0/R_0=1$. On the other hand, when $R(x)>0$ everywhere, the boundary condition $\psi=0$ prevents the existence of a zero eigenvalue—for $\lambda=0$, the equation $(\partial_x^2\psi)/\psi=(\partial_x^2 R)/R$ cannot be fulfilled with $R>0$ and $\psi=0$ at the boundaries.

It is instructive to investigate the change in the phase profile $\varphi(x)=\psi(x)/R(x)$ associated with the lowest eigenvalue as the latter approaches zero. To do that, consider our second test problem (3.10) of Sec. III A,

$$R(x)=\cos[\beta\pi(x-L/2)/L]\ ,\quad V=-\beta^2\pi^2/L^2\ .$$

The "ground state" eigenfunction for the lowest eigenvalue $\lambda_1=1-\beta^2$ is $\hat{\psi}_1(x)=\sin(\pi x/L)$ and

$$\hat{\varphi}_1(x)=\frac{\sin(\pi x/L)}{\cos\left[\beta\pi\dfrac{x-L/2}{L}\right]} \tag{3.18}$$

is the associated phase profile (cf. Fig. 1). As β approaches 1 from below, the phase profile (3.18) becomes constant in the bulk of the system. The x range over which $\hat{\varphi}_1(x)$ drops from 1 in the bulk to zero at the ends shrinks to zero as $\beta\to 1$. Thus, a modulus R dropping to zero at the ends triggers the appearance of a zero eigenvalue with a spatially constant phase mode that does not decay and that allows the pattern to be shifted uniformly along x—for decreasing amplitudes at the ends, the phase pinning of the pattern becomes weaker and weaker: pattern translation costs less and less "energy."

From a formal point of view one might argue that the appearance of a zero eigenvalue in the long-time approximation (2.10) and (3.14) requires—if one insists on not going beyond the framework of the GLE—including the time dependence of the modulus. This, however, does not produce decay of all phase perturbations: Integrating numerically the full GLE (2.5a) with an initial phase perturbation, one easily verifies that any constant spatially homogeneous part of it does not decay, while the nonuniform part decays as predicted by the phase equation (2.10). In Sec. V B we shall present arguments that the appearance of a zero eigenvalue which shows up via nonexponential phase dynamics in fact signals the breakdown of the GLE.

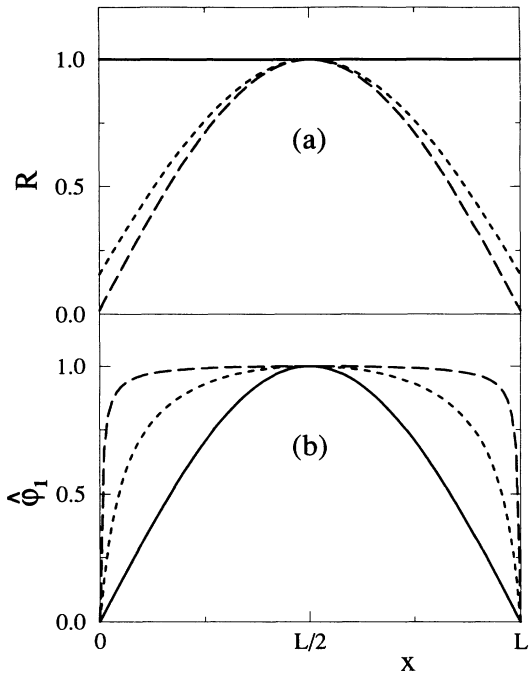

FIG. 1. (a) Test modulus profiles $R(x)=\cos[\beta\pi(x-L/2)/L]$ (3.10a); (b) associated eigenfunctions $\hat{\varphi}_1(x)=\sin(\pi x/L)/R(x)$ for the lowest eigenvalue $\lambda_1=D/D_0=1-\beta^2$, for $\beta=0$ (solid line), 0.9 (long-dashed line), and 0.99 (short-dashed line).

C. Obtaining eigenvalues by a commutation relation

Consider a potential $V(x)$ for which the "Hamilton" operator

$$H=-\partial_x^2+V(x) \tag{3.19}$$

has a zero eigenvalue

$$H\psi_0(x)=0\ . \tag{3.20}$$

Then the potential is related via

$$V(x)=[\partial_x^2\psi_0(x)]/\psi_0(x) \tag{3.21}$$

to the eigenfunction $\psi_0(x)$ associated to the zero eigenvalue. In our context,

$$\psi_0(x)=R_0(x) \tag{3.22}$$

would be a modulus profile that vanishes at $x=0,L$.

Introducing a generalized "creation" operator Q^+ and an "annihilation" operator Q^- by

$$Q^{\pm}=-\left[\frac{\partial_x\psi_0(x)}{\psi_0(x)}\pm\partial_x\right]\ , \tag{3.23}$$

one can write

$$H=Q^+Q^-\ . \tag{3.24}$$

Now consider the new operator

$$\tilde{H}=Q^-Q^+=-\partial_x^2+\tilde{V}(x)\ , \tag{3.25}$$

$$\tilde{V}(x)=-\frac{\partial_x^2\psi_0(x)}{\psi_0(x)}+2\left[\frac{\partial_x\psi_0(x)}{\psi_0(x)}\right]^2 \tag{3.26}$$

obtained by commuting Q^+ and Q^-. $\tilde{H}$ is called the commutation partner [38,39] of H. It is easy to see that $\tilde{H}$ and H have the same eigenvalue spectra away from zero, that is, in the equations

$$H\psi_\lambda(x)=\lambda\frac{\pi^2}{L^2}\psi_\lambda(x),\quad \tilde{H}\tilde{\psi}_\lambda(x)=\lambda\frac{\pi^2}{L^2}\tilde{\psi}_\lambda(x)\ , \tag{3.27}$$

λ is the same for $\lambda>0$. The eigenfunctions are related to each other by

$$\tilde{\psi}_\lambda(x)=Q^-\psi_\lambda(x),\quad Q^+\tilde{\psi}_\lambda(x)=\lambda\frac{\pi^2}{L^2}\psi_\lambda(x)\ . \tag{3.28}$$

Furthermore, $Q^-\psi_0(x)=0$ [38], which is necessary to fulfill the conditions of vanishing ψ_s and $\tilde{\psi}_\lambda$ at $x=0,L$ [38]. Thus, having determined the eigenvalues and eigenfunctions of H, one simultaneously has obtained those of $\tilde{H}$.

For our problem we associate with the potential $\tilde{V}(x)$ a modulus function $\tilde{R}(x)$ via

$$\frac{\partial_x^2\tilde{R}(x)}{\tilde{R}(x)}=\tilde{V}(x)\ . \tag{3.29}$$

Then we find from (3.26) that all functions $R_0(x)$ and $\tilde{R}(x)$ which are related to each other via

$$\frac{\partial_x^2\tilde{R}}{\tilde{R}}=-\frac{\partial_x^2R_0}{R_0}+2\left[\frac{\partial_xR_0}{R_0}\right]^2=\frac{\partial_x^2(1/R_0)}{1/R_0} \tag{3.30}$$

lead to the same eigenvalues $\lambda>0$. This holds in particular for the commutation partners

$$R_0(x)\ \text{ and }\ \tilde{R}(x)=\text{const}/R_0(x)\ . \tag{3.31}$$

The above equation allows us to identify all positive eigenvalues of the phase equation for RBC with those for TVF when using modulus profiles resulting from analytical solutions of the GLE (cf. Sec. IV).

D. Numerical methods

The eigenvalue spectrum of the SSE (3.17) can be determined analytically for special modulus profiles and in addition approximately, e.g., with a perturbation expansion around the analytically solvable case (cf. Sec. IV B 2). In general, however, the potential in the SSE (3.17) reflecting the boundary-induced variation of the modulus shows a nontrivial x dependence that does not allow an analytical solution. Therefore, we integrated the equation numerically for a given potential $V(x)$ using a shooting method.

For a bounded potential as in RBC, a single shot goes for a given λ from $x=0$ with $\psi(0)=0$ and $\psi'(0)\neq0$ to $x=L$. The deviation from the correct target position $\psi(L)=0$ vanishes when λ matches an eigenvalue. We have compared our so-obtained results in some cases with earlier calculations done by Ince [41], who presented a solution in the form of a continued fraction. Both methods agree up to the full four digits given by Ince.

When the potential $V(x)$ diverges at the ends as in TVF, we make use of particular properties of the solution. First, the boundary condition $\psi(0)=0=\psi(L)$ requires mirror symmetry of the lowest eigenfunction with respect to $L/2$. Furthermore, bounded $\psi(x)=\varphi(x)R(x)$ needs at least $\psi\sim1/R(x)$ near the ends. Therefore, we shot from the middle of the interval with $\psi(L/2)=1$, $\psi'(L/2)=0$ to a point $x=\delta$ close to zero. Then a fit of the last points extrapolated to $x=0$ is taken as the function whose zeros correspond to eigenvalues. Here the results can be checked for the potential $V(x)=2/\sin^2x-1$ (cf. Sec. IV B 1) and with the solutions of commutation partner potentials (see above).

We have also investigated how accurate our decoupling approximation (2.10) is compared with the solution of the full GLE (2.5). To that end, we integrated (2.5a) using a Crank-Nicholson method. We found no significant deviations of the long-time behavior of (2.5a) from that of the phase equation (2.10).

Finally, we numerically solved the full time-dependent two-dimensional hydrodynamic field equations with realistic boundary conditions for the RB and TC geometry with a finite-difference algorithm (cf. Sec. V). The explicit finite-difference scheme is described in Ref. [36]. However, the solution method for the Poisson equation was different. Here, the pressure and velocity fields were adjusted iteratively to each other, as reported in [40]. All those calculations gave a coherent picture of the diffusive behavior, which we shall discuss in detail in Secs. IV and V.

IV. APPLICATION OF THE PHASE EQUATION TO RBC AND TVF

In this section we first review the stationary modulus profiles obtained from the GLE for boundary conditions appropriate to RBC and TVF. Then the influence of these modulus profiles on the long-time phase dynamics is discussed within the framework of the phase equation of Sec. III.

A. Stationary modulus profiles resulting from the GLE

The GLE (2.5) has stationary phase winding solutions

$$A(x)=Re^{i\phi(x)}\ , \tag{4.1a}$$

with a phase

$$\phi(x)=\phi_0+(k-k_c)x\ , \tag{4.1b}$$

describing a pattern with a spatially constant wave number k only if the modulus is constant,

$$R=\left[\frac{\epsilon-\xi_0^2(k-k_c)^2}{g}\right]^{1/2}\ . \tag{4.1c}$$

Hence with boundary-induced deviations of $R(x)$ from (4.1c), the solution (4.1) is not possible. However, one obtains profiles $R(x)$ that satisfy the boundary conditions with constant phase ϕ_0—the boundaries cause the family of the phase-winding solutions (4.1) to collapse to k_c [34].

The solutions with constant phase which are discussed here are found by a transformation of the interval $[0,L]$

to $[0,2K]$. Here, $K(m)$ is an elliptic integral of the first kind [42] which is half the periodicity length of the Jacobian elliptic function (JEF). The parameter $m \in [0,1]$ and with it $K(m)$ depend on $\alpha = \sqrt{\epsilon} L/\xi_0$ (2.9), which in turn is fixed by the particular combination of control parameter ϵ and system length L. The relation between m, $K(m)$, and α is

$$\alpha = 2K(m) \times \begin{cases} \sqrt{1-2m} & \text{for } 0 < \alpha < \pi \\ \sqrt{1+m} & \text{for } \pi \leq \alpha \ . \end{cases} \tag{4.2}$$

The resulting m and K are shown in Fig. 2 as a function of α.

1. R(x) and V(x) for TVF

For TVF with diverging amplitude at the ends [25], the JEF's ds and ns [42] solve the GLE with convex modulus profiles [cf. Fig. 3(a)]:

$$R(x) = \begin{cases} R_\infty \left[\dfrac{2}{1-2m} \right]^{1/2} \mathrm{ds}\left[2K\dfrac{x}{L} \middle| m \right] & \text{for } 0 < \alpha < \pi \\ R_\infty \left[\dfrac{2}{1+m} \right]^{1/2} \mathrm{ns}\left[2K\dfrac{x}{L} \middle| m \right] & \text{for } \pi \leq \alpha \ . \end{cases} \tag{4.3a}$$

(4.3b)

Here,

$$R_\infty = \sqrt{\epsilon/g} \tag{4.4}$$

is the modulus in a system of infinite extent. The prefactor in front of both JEF's can also be expressed as $(\xi_0/\sqrt{g})(2K/L)\sqrt{2}$. This shows that $R(x)$ is a function only of α and L. The minimal modulus at $x = L/2$ is

$$R(x = L/2) = \begin{cases} R_\infty \left[2\dfrac{1-m}{1-2m} \right]^{1/2} & \text{for } 0 < \alpha < \pi \quad (4.5a) \\ R_\infty \left[\dfrac{2}{1+m} \right]^{1/2} & \text{for } \pi \leq \alpha \ . \quad (4.5b) \end{cases}$$

With α increasing beyond π, the parameter m rapidly approaches 1 (cf. Fig. 2) so that already for $\alpha = 10$, the minimum is larger than R_∞ by only 0.34%.

The potential $V = (\partial_x^2 R)/R$ corresponding to the above modulus (4.3),

$$V(x) = \frac{\epsilon}{\xi_0^2} \left[\frac{R^2(x)}{R_\infty^2} - 1 \right] = \left[\frac{2K}{L} \right]^2 \times \begin{cases} 2\,\mathrm{ds}^2\left[2K\dfrac{x}{L} \middle| m \right] + 2m - 1 \ , & 0 < \alpha < \pi \\ 2\,\mathrm{ns}^2\left[2K\dfrac{x}{L} \middle| m \right] - m - 1, & \pi \leq \alpha \ , \end{cases} \tag{4.6}$$

is positive everywhere and convex [cf. Fig. 3(b)]. The relation (4.6) reflects the fact that R is a JEF solving the GLE so that $(\partial_x^2 R)/R$ is related to R^2.

2. R(x) and V(x) for RBC

For RBC with vanishing modulus at both ends, the threshold for onset is shifted [32] upwards from $\epsilon_0(L = \infty) = 0$ to $\epsilon_c(L) = \pi^2 \xi_0^2 / L^2$ corresponding to $\alpha_c = \pi$. Thus, $R(x) = 0$ for $\alpha < \pi$, while above the threshold α_c one finds the solution [cf. Fig. 4(a)]

$$R(x) = R_\infty \left[\frac{2m}{1+m} \right]^{1/2} \mathrm{sn}\left[2K\frac{x}{L} \middle| m \right] = \frac{\xi_0}{\sqrt{g}} \frac{2K}{L} \sqrt{2m}\, \mathrm{sn}\left[2K\frac{x}{L} \middle| m \right] . \tag{4.7}$$

The maximal value at $x = L/2$,

$$R(x = L/2) = R_\infty \left[\frac{2m}{1+m} \right]^{1/2} , \tag{4.8}$$

varies close to α_c, i.e., close to $m = 0$, proportional to $(\alpha - \alpha_c)^{1/2}$, as can be seen from Fig. 2, and reaches R_∞ from below for $m \to 1$. The potential $V(x)$ associated with (4.7),

$$V(x) = \frac{\epsilon}{\xi_0^2} \left[\frac{R^2(x)}{R_\infty^2} - 1 \right] = \left[\frac{2K}{L} \right]^2 \left[2m\, \mathrm{sn}^2\left[2K\frac{x}{L} \middle| m \right] - m - 1 \right] , \tag{4.9}$$

has the same formal dependence on R as for the TVF case. Note, however, that $V(x)$ for RBC is partly con-

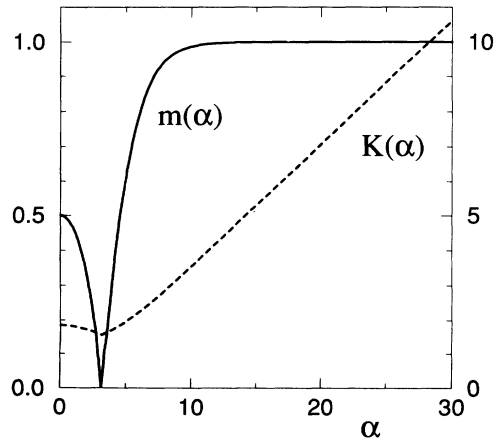

FIG. 2. Parameters m (solid line and left ordinate) and $K(m)$ (dashed line and right ordinate) as functions (4.2) of $\alpha = \sqrt{\epsilon} L/\xi_0$.

vex and partly concave but negative everywhere [cf. Fig. 4(b)].

For later use we mention here that the potential (4.6) for TVF is, for $\alpha \geq \pi$, a commutation partner of the potential (4.9) for RBC: Comparing (4.3b) with (4.7), one finds

$$R_{\mathrm{TVF}}(x)=\mathrm{const}/R_{\mathrm{RBC}}(x) \ . \tag{4.10}$$

3. *Comparison with numerical simulations of the field equations*

In Fig. 3 we show a representative example of the modulus profiles for TVF (4.3b) and in Fig. 4 one for RBC (4.7) in comparison with the envelope of velocity fields taken from our numerical simulations (see Sec. V) of the full field equations. In addition, we show the corresponding potentials $V(x)$ (4.6) and (4.9). Generally one can say that the modulus profile (4.7) for RBC agrees much better with that of the simulation than the modulus profile (4.3) of TVF. This has two reasons: The GLE is a very good model for RBC [26,27], even if ϵ is not infinitesimal, while for TVF, the cylindrical geometry leads to an inflow-outflow asymmetry which strongly restricts the ϵ range of validity of the GLE [22,30]. The second point is that the boundary condition $A=0$ for RBC is fulfilled also at larger ϵ, whereas $A=\infty$ for TVF need not be the correct one for higher ϵ [25]. For these reasons we always use in the RBC case the theoretical $R(x)$ (4.7) as input into the phase equation. In the TVF case we also use for $R(x)$ a fit to the final stationary TVF amplitude profiles from our numerical simulations.

B. Effective diffusion constants

Here we determine the spectrum of eigenvalues and in particular the lowest ones of (3.2) and (3.17) by using the analytical modulus profiles resulting from the GLE. For RBC with a modulus (4.7) that drops to zero at both ends, there is a zero eigenvalue which does not occur for TVF. However, apart from that, all positive eigenvalues in the RBC and TVF case are identical when $\alpha \geq \pi$ because of the commutation relationship (3.31) of the moduli (4.10). Hence, having obtained the effective diffusion constant from the smallest *nonvanishing* eigenvalue, e.g., for the RBC modulus, we also have the diffusion constant for the TVF case, or vice versa.

1. *Eigenvalues for* $\alpha=\pi$

The complete eigenvalue spectrum of the phase equation can be determined analytically at $\alpha=\pi$, i.e., $m=0$

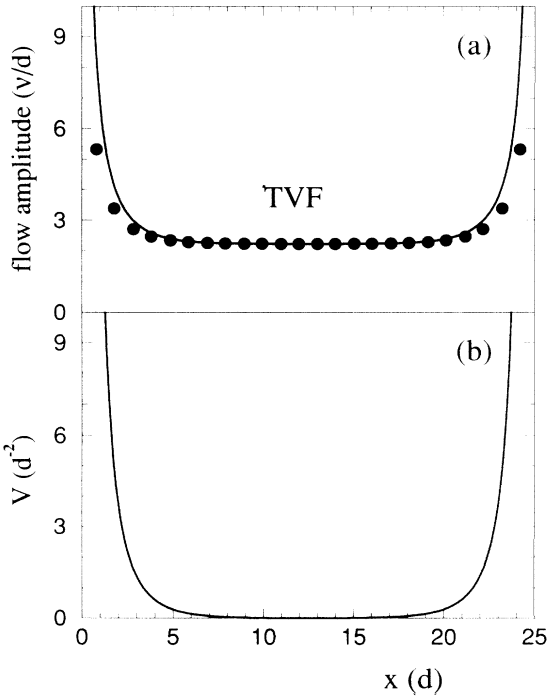

FIG. 3. (a) Axial profile of TVF amplitudes. The circles denote the intensity envelope of the axial velocity field $w(r_1+d/4,x)$ close to its maximum obtained from a numerical simulation of the full axisymmetric Navier-Stokes equations with boundary conditions corresponding to rigid, nonrotating end plates at $x=0,L$. The solid line represents the solution $R(x)$ (4.3b) of the GLE scaled so as to coincide with w at $x=L/2$. (b) Potential $V(x)=[\partial_x^2 R(x)]/R(x)$ (4.6) corresponding to the modulus profile of the GLE. The parameters are $\eta=0.75$, $\epsilon=0.0167$, $L=25d$, and $\alpha=12.10$.

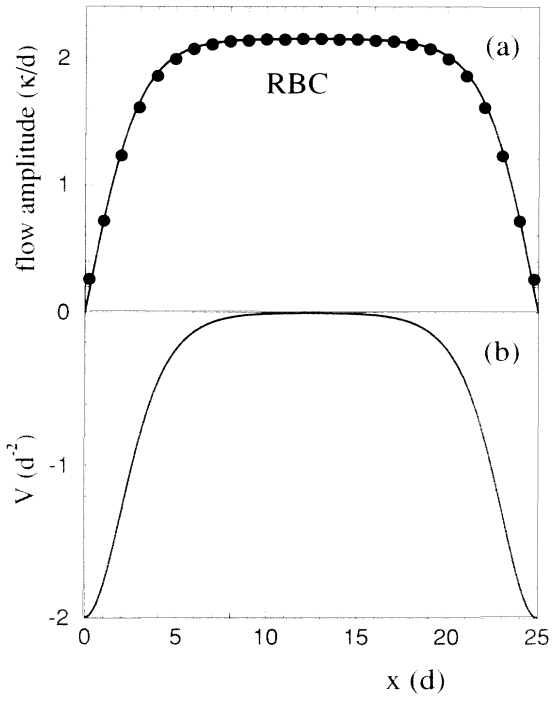

FIG. 4. (a) Lateral profile of RBC amplitudes. The circles denote the intensity envelope of the vertical velocity field $w(x,z=d/2)$ at midheight of the fluid layer obtained from a numerical simulation of the 2D Oberbeck-Boussinesq equations with a linear vertical temperature variation imposed at the ends at $x=0,L$. The solid line represents the solution $R(x)$ (4.7) of the GLE scaled so as to coincide with w at $x=L/2$. (b) Potential $V(x)=[\partial_x^2 R(x)]/R(x)$ (4.9) corresponding to the modulus profile of the GLE. The parameters are $\mathrm{Pr}=1$, $\epsilon=0.035$, $L=25d$, and $\alpha=12.15$.

and $K=\pi/2$. There the modulus of RBC vanishes with $m\to 0$, while its profile

$$\mathrm{sn}(2Kx/L|m)\to\sin(\pi x/L)\ ,$$

so that

$$[\partial_x R(x)]/R(x)\to(\pi/L)\cot(\pi x/L)\ .$$

For the TVF case one has $R(x)\sim 1/\sin(\pi x/L)$ at $\alpha=\pi$. Thus,

$$V_{\mathrm{RBC}}=-\frac{\pi^2}{L^2},\quad V_{\mathrm{TVF}}=\frac{\pi^2}{L^2}\left[\frac{2}{\sin^2(\pi x/L)}-1\right], \tag{4.11}$$

and the reduced eigenvalues of $H=-\partial_x^2+V(x)$ (3.17) are

$$\lambda_n=n^2-1\ , \tag{4.12}$$

where $n=1,2,\ldots$ for RBC and $n=2,3,\ldots$ for TVF. The eigenfunctions are

$$\psi_n=\begin{cases}|n\rangle & \text{for RBC } (n=1,2,\ldots)\\ Q^-|n\rangle & \text{for TVF } (n=2,3,\ldots)\ ,\end{cases} \tag{4.13}$$

with $|n\rangle=\sqrt{2/L}\sin(n\pi x/L)$ and

$$Q^{\pm}=-\left[\frac{\partial_x R}{R}\bigg|_{\mathrm{RBC}}\pm\partial_x\right]=-\left[\frac{\pi}{L}\cot\left[\pi\frac{x}{L}\right]\pm\partial_x\right]\ . \tag{4.14}$$

Here we have used $H_{\mathrm{RBC}}=Q^+Q^-$ and $H_{\mathrm{TVF}}=Q^-Q^+$. Note the different normalization of the eigenfunctions in (4.13).

The effective diffusion constant obtained in both cases from $\lambda_2=3$,

$$D(\alpha=\pi)=3D_0\ , \tag{4.15}$$

is three times as big as in an unbounded system. Note that (4.15) is an exact result of our phase equation for moduli profiles of the GLE.

2. *Solution for arbitrary α*

While for $\alpha=\pi$, where the JEF's degenerate to trigonometric functions, an exact analytical result is available, we have solved the general case $\alpha\neq\pi$ numerically. As an aside, we mention that we have also evaluated the eigenvalues for $\alpha\neq\pi$ with a straightforward perturbation expansion around $\alpha=\pi$. We found that this approximation breaks the commutation partnership of RBC and TVF: The lowest RBC eigenvalue no longer vanishes for $\alpha>\pi$ and the higher ones of RBC and TVF differ within lowest order perturbation theory. The latter, by the way, agrees better for TVF than for RBC with our numerical results (cf. below)—the deviation of D/D_0 at $\alpha=10$ is 0.6% for TVF and 20% for RBC.

The numerically exact solution of the eigenvalue problem (3.17) with the potentials (4.6) and (4.9) was obtained with a shooting method, as described in Sec. III D. For TVF, the two branches, $\alpha<\pi$ and $\alpha>\pi$, were checked against each other using the relation

$$\mathrm{ds}^2(x|m)=\mathrm{ns}^2(x|m)-m$$

Ref. [42]. A further test for $\alpha\gtrsim\pi$ is that the nonzero eigenvalues of TVF and RBC have to be identical due to the commutation relation. The numerical data coincide up to 10^{-7}, the precision of the integration scheme.

The effective diffusion constants resulting from the numerically obtained lowest eigenvalue of (3.17) are shown in Fig. 5. For TVF the full range of α starting at $\alpha=0$ is applicable, albeit experimentally realized parameter combinations are $\alpha\gtrsim 10$. For RBC, α has to be above the threshold for onset, $\alpha_c=\pi$. The limiting value for vanishing α, meaning ϵ going to zero for a short container length, is $D/D_0\ (\alpha\to 0)=3.3833$ [41]. This is also the overall maximum. The curve is strictly decreasing with a turning point at $\alpha=\pi$, $D/D_0=3$. For high α, say, $\alpha\gtrsim 20$, a good approximation is given by

$$D/D_0\ (\alpha\to\infty)\simeq 1+\frac{12.8261}{\alpha^{1.204}}\ .$$

The function approaches 1 very slowly. Even for $\alpha=100$, which is higher than in all experimental setups in the literature, D lies with 5% detectably above D_0.

Let us summarize the main predictions of our theory of the long-time phase dynamics based upon Eqs. (2.10) and (3.14) together with the JEF modulus profiles of the stationary GLE:

(i) The phase dynamics depends only on the parameter $\alpha=\sqrt{\epsilon}L/\xi_0$ but not on ϵ and L separately.

(ii) For a fixed common α, the spectrum of the positive eigenvalues of the phase equation is identical for the RBC and TVF modulus profiles given by JEF's.

(iii) The long-time *exponential* relaxation of the phase governed by the smallest *nonzero* eigenvalue is markedly enhanced by the boundary-induced amplitude variation

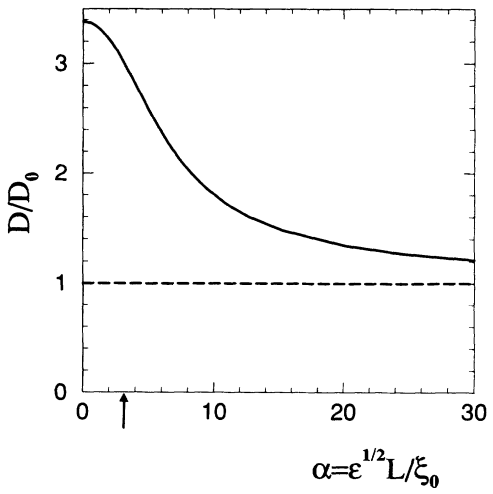

FIG. 5. Effective diffusion constants D/D_0 for RBC and TVF in finite systems as function of $\alpha=\sqrt{\epsilon}L/\xi_0$ obtained by numerical integration of the eigenvalue equations (3.17) with potentials taken from the GLE [(4.6) and (4.9)]. The arrow marks $\alpha=\pi$ where $D/D_0=3$ is known analytically. For $\alpha<\pi$ there exists TVF but no RBC.

as compared to the unbounded system—the effective diffusion constant D is for experimentally relevant parameters significantly larger than D_0, e.g., $D/D_0=1.35$ at $\alpha=20$.

(iv) For the RBC modulus profile which vanishes at the sidewalls, a zero eigenvalue appears. Then within the phase equation (2.10) as well as within the full GLE dynamics of (2.5), a spatially constant contribution to the initial phase perturbation does not decay.

In Sec. V we discuss how results (i)–(iv) help understand and explain experiments and numerical simulations of the full field equations and how well they agree.

V. COMPARISON WITH EXPERIMENTS AND NUMERICAL SIMULATIONS

After having discussed our theory of the long-time phase dynamics, we shall compare in this section the predictions of the phase equation using GL amplitude profiles as input with experimental results available in the literature and with our own numerical simulations. For the sake of a detailed comparison and investigation of the long-time phase dynamics, we decided to solve the full hydrodynamic field equations for the TC system as well as for the RB system numerically with a finite-difference algorithm [36,40]. In particular, for RBC these simulations turned out to be very fruitful in elucidating the consequences of the existence of a zero eigenvalue in the GLE and in interpreting the experimental results. We shall start with the less complicated TVF.

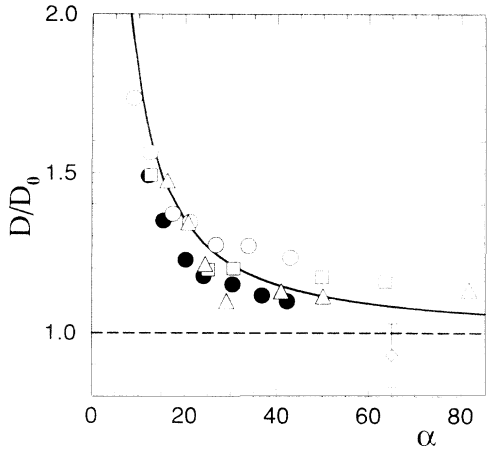

FIG. 6. Effective diffusion constant D/D_0 of TVF patterns in finite systems versus $\alpha=\sqrt{\epsilon}L/\xi_0$. The solid circles result from our numerical simulations of the full axisymmetric NSE in TC setups of length $L=25d$ and radius ratio $\eta=0.75$. The open symbols denote experimental results of Gerdts [19] in systems of length $L/d=8.3$ (circles), 12.3 (squares), and 20.3 (triangles) with $\eta=0.5$. The open diamond with its error bar is the result of Wu and Andereck [20] for $k=k_c$. The solid line represents our phase equation theory (Fig. 5) with modulus profiles $R(x)$ (4.3) of the GLE taken as input. D_0 is the phase diffusion constant in the corresponding unbounded setups as described in the text.

A. Taylor-Vortex flow

1. Experiments

The experimental setup and procedure that Gerdts [19] used to characterize the long-time relaxation of the vortex positions have already been described in Sec. II. He used cylinders of radius ratio $\eta=0.5$ with different lengths $L/d=8.3$, 12.3, and 20.3. In each case the outer cylinder was stationary and the annulus was closed by two nonrotating end plates. He showed that the relaxation time increased with growing L and decreasing ϵ and that the equilibration process was of diffusive nature. The underlying universal physical law becomes clearer when considering the data as a function of α.

So, in Fig. 6 we compile in a plot of D/D_0 versus α all data of his work (open symbols) which are compatible with our restrictions that the variation of the local wave number is negligible and that the deviation of the final bulk wave number k from k_c is small. For the normalization of the experimental data, we used the theoretical diffusion constants $D_0(\epsilon,k)$ determined by Riecke [7] for TVF patterns with uniform final wave number k in an unbounded TC system of radius ratio $\eta=0.5$. Except for one experimental runaway ($D/D_0=4.8$ at $L=12.4d$, $\epsilon=0.002$, $\alpha=2.1$), which lies far outside the plot range, the Gerdts results covering an α range up to 80 thread along the full theoretical line in Fig. 6. The latter follows from the phase equations (2.10) and (3.14) with the TVF modulus profile (4.3) resulting from the analytical solution of the GLE. While for small α the experimental diffusion constants seem to lie below the full line they show a clear enhancement over D_0 by factors up to 2.

We are aware of one further experimental work, by Wu and Andereck [20], where the phase of Taylor vortices is perturbed by end plate motion. However, the authors analyzed the relaxation behavior by an error function rather than exponentials so that their result is affected by more than the smallest eigenvalue. In a system of $\alpha=65$, $\eta=0.882$, they report for a TVF pattern with the critical wave number an effective diffusion constant $D/D_0=0.93\pm0.10$ (open diamond in Fig. 6), while our theoretical value would be 1.08. All their other diffusion coefficients are obtained for patterns with wave numbers away from k_c ($0.09\le|k-k_c|\le0.36$). Nevertheless, we find it surprising that for all of them, D/D_0 is below 1, albeit with large error bars. The response to a periodic phase disturbance that was investigated experimentally in the same reference [20] will be discussed in Sec. VI.

2. Numerical simulations

In our simulations we solved the time-dependent axisymmetric Navier-Stokes equations (NSE) in the r-x cross section of the annulus between a rotating inner cylinder, a nonrotating outer cylinder, and nonrotating rigid-end boundaries at $x=0,L$, using an explicit finite-difference scheme described in [36,40]. The radius ratio $\eta=0.75$ and the system length $L=25d$ were kept fixed

for all runs. Varying ϵ between 0.017 and 0.207, we covered the range $12.1 \leq \alpha \leq 42.2$. In direct analogy to the experimental procedure of Gerdts [19], we monitored the time evolution of the vortex positions after a small movement by $0.2d$ of an end plate. The long-time diffusive character of the phase dynamics and the fact that it is dominated by one spatial mode were explicitly checked by investigating the relaxation behavior of several vortex positions. Typically the long-time relaxation rate $\gamma_{\min}$ of the vortex positions was determined from an interval of 450 to 500 radial diffusion times after the movement of the end plate. The resulting effective diffusion constant $D = \gamma_{\min} L^2/\pi^2$ was reduced by the theoretical value $D_0(\epsilon, k)$ [7] for relaxation in an infinite system to a pattern with spatially constant modulus and constant wave number k. Here k was taken as the numerical wave number in the bulk of our finite system. Our numerical bulk wave numbers differed at most by 7% from the critical one, k_c.

The effective diffusion constants from the numerical simulations (solid circles in Fig. 6) lie consistently below the solid curve. The reason for this shortcoming of the phase equation with modulus input from the GLE seems to be the GLE modulus rather than the phase equation itself—the deviation of the GLE modulus from the numerical intensity profile of, e.g., the axial velocity field $w(r = r_1 + d/4, x)$ is quite obvious in Fig. 3(a). The above hypothesis was tested in two different ways: First, instead of using in the JEF (4.3) the parameter m as fixed by our specific numerical ϵ or α values, we treated m as an arbitrary fit parameter. Its optimal value was determined by a best fit of $R(x)$ (4.3) with weights varying inversely with the distance from both ends to the numerically obtained intensity profile of w. Inserting this fitted modulus into the phase equation, the resulting diffusion constants practically agreed with the solid dots in Fig. 6. The deviation is $\sim 5\%$ for small α and shrinks continuously to values less than 1%. Second, we compared with results of previous work [22]. There the input modulus into the phase equation was obtained from a cubic spline through the extrema of the simulated radial velocity field with a vanishing second derivative at the ends that led to finite moduli there. The resulting effective diffusion constant $D/D_0 = 1.19$ [22] for $\alpha = 20.12$ ($\epsilon = 0.047$) compares well with $D/D_0 = 1.23$ from the full numerical simulation, where $D/D_0 = 1.32$ is the theoretical value with the GLE modulus.

From all this we conclude that the phase equations [(2.10) and (3.14)] properly and quantitatively describe the long-time TVF phase dynamics provided the right modulus profile $R(x)$ is used as input.

B. Rayleigh-Bénard convection

1. Experiments

Croquette and Schosseler [17] performed experiments to demonstrate the applicability of a diffusion equation for describing the long-time phase dynamics of RBC. They enforced a convection pattern with a spatially varying wave number by shining powerful light through an appropriate grid onto the convection cell, i.e., by imposing temperature variations that were an image of the grid. After removal of the light source, the bulk pattern evolved into regularly spaced rolls. From this time evolution the authors inferred effective diffusion constants $D = 0.76D_0$ and $0.83D_0$ in a slightly different setup.

For the same parameters ($\epsilon = 0.6$, $L = 20$, $\alpha \simeq 40$) the phase equation with the GL modulus input yields beyond the zero eigenvalue an *exponential* time relaxation, leading to an effective diffusion constant $D = 1.14D_0$. We shall now investigate this seeming discrepancy between experiments and phase equation approach by analyzing in detail numerical simulations of the field equations. In particular, we want to elucidate the question of whether and how the zero eigenvalue in the GL dynamics also appears in the full field equations.

2. Numerical simulations

For the RBC system we solved the 2D velocity and temperature field equations in Oberbeck-Boussinesq approximation in a vertical cross section of the fluid layer perpendicular to the axes of the convective rolls. The Prandtl number of the fluid was $\mathrm{Pr} = 1$. At the rigid lateral boundaries we imposed the linear vertical conductive temperature profile between the hot bottom plate and the cold top plate. Thus the amplitudes of the velocity field as well as of the convective temperature field vanish there. Consequently, the phase of the pattern is not fixed and the mechanism to generate phase perturbations by end walls does not work properly. Instead, we induced a continuous phase perturbation that was largest in the center and decreased towards the ends, causing an inhomogeneous sidewards displacement of the whole pattern in the positive x direction, as shown in Fig. 7(a) by the local deformation Δx versus x. In this way rolls in the right (left) part of the system are squeezed (stretched) as indicated in Fig. 7(b). There we plot the initial, perturbed distances $x_n - x_{n-1}$, between adjacent node positions of the vertical velocity field $w(x, z = \frac{1}{2}, t = 0)$ at midheight of the fluid layer versus $(x_n + x_{n-1})/2$. The node positions x_n locate the roll centers.

The typical response to this initial perturbation is shown in Fig. 8 for a system of $L = 25d$ with 25 convection rolls. There the time evolution of the tenth node position, x_{10}, is shown over 13 000 vertical diffusion times d^2/κ corresponding to 20 lateral diffusion times L^2/κ. Three values of ϵ are chosen to demonstrate the varying ranges of different dynamical behavior. Consider first the solid line when ϵ is smallest. After a short period of strong decrease of $x_{10}(t)$ which is finished at about $t = 20d^2/\kappa$, the rolls move linearly for nearly 8000 diffusion times. Eventually, the space-time curve $x_{10}(t)$ bends and, taking more and more exponential shape, relaxes towards the final position. Both the speed of the linear motion v_{lin} and the final decay rate $\bar{\gamma}$ are extremely small. If one increases ϵ to 0.035 (long-dashed lines), this behavior goes faster and, in particular, the range of linear motion is squeezed. For $\epsilon = 0.1$, it is hard to detect such a linear motion: The node position seems to relax immediately exponentially. At first sight one is tempted to identify the ultra-long-time decay rates $\bar{\gamma}$ appearing, e.g., for $\epsilon = 0.015$, around 10 000 diffusion times with a

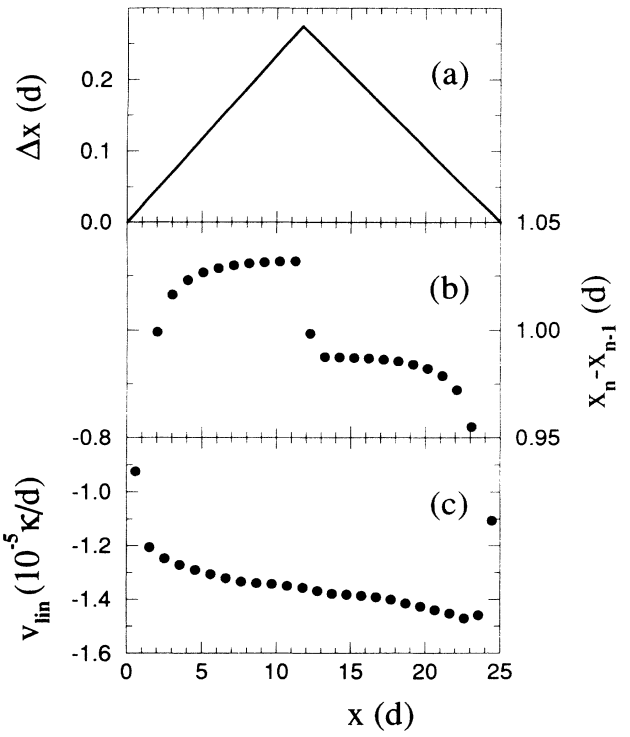

FIG. 7. Phase deformation of a RBC pattern in a system of length $L=25d$: (a) Initial shift Δx of the pattern, (b) resulting initial distances $x_n - x_{n-1}$ between adjacent nodes of $w(x,z=\frac{1}{2})$, and (c) restoring velocity v_{lin} of the node positions in the time interval of linear motion (cf. the text).

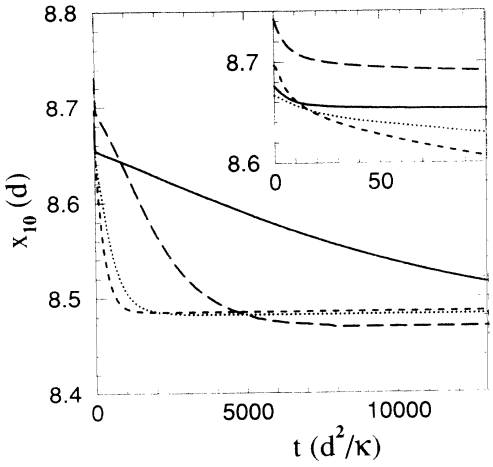

FIG. 8. Relaxation of an initial phase perturbation (cf. the text and Fig. 7) in RBC obtained from numerical simulations of the full field equations for Pr=1 with rigid sidewalls at $x=0$ and $25d$. There we imposed vertically the linear conductive temperature profile with $\epsilon=0.015$ (solid line), $\epsilon=0.035$ (long-dashed line), and $\epsilon=0.1$ (dashed line), or we imposed a perfectly heat isolating boundary condition $\partial_x T=0$ for $\epsilon=0.015$ (dotted line). We plot the position $x_{10}(t)$ of the tenth node of the vertical velocity field at midheight corresponding to the center of the tenth roll. The insert magnifies the strong changes within the first 100 vertical diffusion times.

diffusive eigenvalue. The rates, however, are much too small compared with γ_0 (cf. Table I). A more important argument against a diffusive behavior is that the ultra-long-time relaxation contains only a single spatiotemporal mode, whereas diffusion contains several modes (2.3) with decay rates increasing quadratically with the mode index—attempts to fit $x_n(t)$ with more than one exponential function failed.

We think that the proper (higher) diffusive modes can be identified by carefully analyzing the first 100 vertical diffusion times and that all subsequent events in Fig. 8 can be explained as consequences of the presence of a zero eigenvalue in the phase equation (3.2). A zero eigenvalue implies that a spatially homogeneous phase perturbation, once introduced into the system, is not damped within the frame of the phase equation (3.2) and also of the GLE (2.5) as discussed in Sec. III B 2. Indeed, if one integrates numerically the GLE (2.5) with an initially nonuniform phase profile, one can see diffusive relaxation with spatiotemporal modes as predicted by the phase equation (3.2). But any constant part of the initial deviation is not carried away at all. Thus, in the system de-

TABLE I. Velocity of the linear motion v_{lin}, ultra-long-time relaxation rate $\bar{\gamma}$ of the 14th node position, and effective diffusion constant D obtained from numerical simulations of RBC with rigid sidewalls imposing the conductive temperature profile there. The values in parentheses result from an initial perturbation which has half the strength.

α	ϵ	v_{lin} ($10^{-5}\kappa/d$)	$10^2\bar{\gamma}/\gamma_0$	D/D_0
8.0	0.015	1.4 (0.73)	0.43	2.16 (2.16)
8.6	0.015	0.63		2.06
10.3	0.025	3.9 (1.9)	1.3 (1.2)	1.84 (1.86)
12.1	0.035	6.3 (6.1)	2.2 (2.4)	1.69 (1.71)
14.5	0.05	13.5 (12.9)	3.9 (4.5)	1.54 (1.58)
17.8	0.075		8.7 (8.7)	1.60 (1.64)
18.9	0.1		12.5	1.70
20.5	0.1		13.3 (13.3)	1.52 (1.66)
22.2	0.1		14.2	1.56
29.0	0.2		28.6	
40.2	0.383		49.5	

scribed by the full field equations, there must be a restoring mechanism which is not captured by the GLE. It drives—after the higher spatially varying diffusive modes of the initial phase perturbation have died out—the remaining spatially homogeneous bulk part of the roll displacements into a global, almost constant, restoring motion. Its speed is almost constant in space [cf. the bulk part of Fig. 7(c)] and time [cf. the linear range of $x_{10}(t)$ in Fig. 8] because of the zero eigenvalue that would allow a perfectly free motion within the GLE. Eventually, when the rolls approach their final position, the motion is slowed down until the equilibrium state is reached that was prepared prior to the phase perturbation. The reason for all this behavior seems to be an interaction between the phase and the lateral borders in the full system which prohibits a roll from being pushed out of the system. The strength of that interaction responsible for the linear motion and the final overdamped approach to the equilibrium position depend on the system parameters ϵ and L, as one can infer from Table I. There we have compiled the speed of a particular roll position in the range of linear motion, $v_{\rm lin}$, and its ultra-long-time relaxation rate $\tilde{\gamma}$. While $\tilde{\gamma}$ is almost independent of x, i.e., the same for every roll, $v_{\rm lin}$ varies slightly along x and increases towards the region of largest initial compression [cf. Fig. 7(c)]. Since the entire behavior lies beyond the GLE, we are not able to make theoretical predictions about the dependence of $\tilde{\gamma}$ or $v_{\rm lin}$ on ϵ and L.

Prior to this ultraslow long-time dynamics, as a consequence of the zero eigenvalue of the GLE, it is possible to analyze the dynamics related to the higher, diffusive eigenvalues of Eqs. (2.10) and (3.14). In order to eliminate most of the global motion, we now investigate the temporal behavior of the distance between two adjacent nodes. We fit the data of Fig. 9 beyond an initial time interval of about $20d^2/\kappa$ to an exponential plus a longer lasting function—a linear one or an additional exponential corresponding to the ultraslow behavior in Fig. 8. The relaxation rate of the first exponential gives us D/D_0. To check for nonlinear dependences on the initial phase perturbation, we have made a second series of simulations where the initial perturbation was half of that before. In Table I, the resulting values are printed in brackets. The speed of the linear motion, $v_{\rm lin}$, deviates up to a factor of 2, which seems to indicate a nonlinear force. On the other hand, with $\tilde{\gamma}$ and D differing only by few percent, these exponential dynamics suggest a linear mechanism.

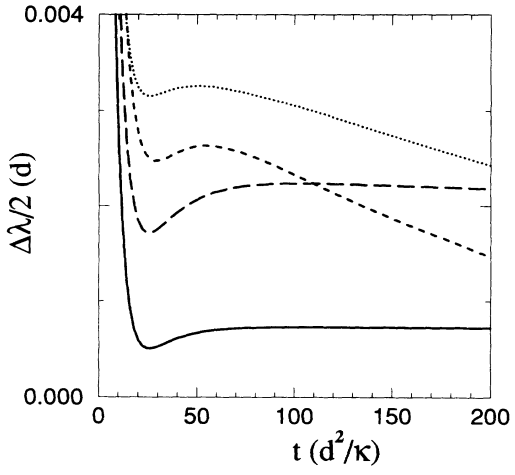

FIG. 9. Adjustment of the local wavelength in RBC taken from numerical simulations of the full field equations. The plot shows the deviation $\Delta\lambda(t)$ of the local wavelength from its final value $\lambda(t\rightarrow\infty)$ determined from the difference between the tenth and the ninth node positions of the vertical velocity field. The parameters and line types are the same as in Fig. 8.

In Fig. 10 we have plotted the effective diffusion constants D/D_0 obtained in the above-described way from our simulations of the full field equations together with the theoretical curve (cf. Fig. 5) that represents the lowest nonvanishing diffusive eigenvalue of the phase equation. The lower part of Fig. 10 shows the ultra-long-time relaxation rates $\tilde{\gamma}/\gamma_0$ seen in our simulations. The solid symbols are the results of simulations where, by imposing the conductive state at the lateral boundaries, the convective amplitudes of all fields were enforced to vanish there. The relatively large error bars of the D/D_0 data come from the behavior of different nodes and reflect the complicated extraction method. For $\epsilon > 0.1$, it is impossible to filter out D because the diffusive relaxation becomes comparable to $\tilde{\gamma}$.

At this point, we come back to the experiment of Croquette and Schosseler [17]. Now their result, $D/D_0 = 0.76$ and 0.83, can be understood as effective ultra-long-time relaxation rates $\tilde{\gamma}/\gamma_0$ (stars in Fig. 10)

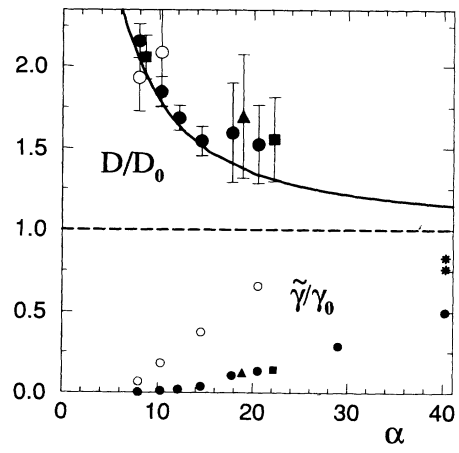

FIG. 10. Relaxation rates of phase perturbations of RBC in finite systems versus $\alpha = \sqrt{\epsilon} L/\xi_0$. Numerical simulations of the full field equations for Pr = 1 with the conductive temperature profile imposed at the lateral boundaries gave the solid circles for $L = 25d$, solid squares for $L = 27d$, and solid triangles for $L = 23d$. The open circles represent a run for $L = 25d$ with perfectly heat isolating boundaries. The stars come from the experiment [17]. The rates labeled D/D_0 in the upper part were obtained on the scale of about 100 vertical diffusion times and are identified by comparison with the phase diffusion theory of Fig. 5 (solid line) as coming from the smallest nonvanishing diffusive eigenvalue. The rates labeled $\tilde{\gamma}/\gamma_0$ in the lower part refer to ultra-long-time dynamics whose appearance is linked to the existence of a zero eigenvalue of the phase equation (cf. the text).

caused by the zero eigenvalue. In our numerical simulation with the conductive state imposed at the boundaries, we got for the same α a relaxation rate $\tilde{\gamma}/\gamma_0=0.5$. Since $\tilde{\gamma}$ does not seem to be a function of $\alpha=\epsilon^{1/2}L/\xi_0$ but rather of ϵ/L, the different ϵ values could have produced the deviation. Furthermore, in an experimental setup the vertical temperature profile at the lateral boundaries is never the pure conductive one as used in the above simulations. Instead, a heat isolating condition $\partial_x T=0$ might be more appropriate if the Prandtl number of the fluid is not too high. Therefore, we also simulated perfectly heat isolating boundary conditions (dotted lines in Figs. 8 and 9 and open circles in Fig. 10). The main result is a larger long-time relaxation rate $\tilde{\gamma}$ which is ~ 10 times faster than in the case of Dirichlet boundaries for T. As a consequence, the extraction of the nonzero diffusive eigenvalues becomes extremely difficult.

We finally should like to mention that the case of rigid heat isolating boundaries cannot be treated properly within our phase diffusion equation since it is based on the assumption that velocity and convective temperature fields can be described by one amplitude only, and this is not the case near a heat isolating rigid sidewall.

VI. PHASE WAVES GENERATED BY PERIODIC FORCING

So far, we have studied the relaxation of an initially applied phase perturbation after, e.g., the movement of an end plate. However, recently experiments have been reported to determine the diffusion constant by imposing a time-periodic disturbance on the system. Wu and Andereck [20], working on TVF, replaced the single-step motion of an end plate with a continuous sinusoidal motion. On the other side, Wesfreid and Croquette [16] injected a vertical, time-periodic stream into the middle of their RB container. Both groups based the analysis of their measured response on the simple diffusion equation (2.1) with homogeneous pattern amplitude and got a value for the diffusion constant close to the theoretical one, D_0.

This analysis uses the fact that in the idealized equation (2.1) for a homogeneous modulus, a time-periodic, spatially localized forcing of the phase generates a damped phase wave propagating away from the perturbation. The experiments then can measure two different and independent quantities characterizing such a type of phase response to a periodic forcing: (i) the local decay length of the amplitude of the damped phase wave that is emitted from the periodic perturbation source and (ii) the local wavelength of the phase wave. The simple diffusion equation (2.1) predicts that both lengths are the same and space-independent:

$$\mathcal{K}_0^{-1}=(2D_0/\omega)^{1/2} , \tag{6.1}$$

in a semi-infinite system, and that they are given by the diffusion constant D_0 and the frequency ω of the modulation. The experimentally obtained decay lengths differed slightly from the wavelengths but the differences were within the error bars of the measurements.

It should be noted, however, that the dynamical properties of damped phase waves emitted by periodically applied forces are in general—if the governing equation for the phase is not an ideal diffusion equation—unrelated to and different from the free diffusive relaxation of an initially prepared phase perturbation.

A. Finite size and amplitude variation effects

Here we investigate the effect of a finite system size and the consequences of a spatially varying pattern intensity $R(x)$ on the phase waves generated by a periodic, spatially localized perturbation of the phase. We treat a situation described by Eq. (3.17) where the periodic modulation basically affects only the phase, while the modulus $R(x)$ of the pattern amplitude and with it the potential $V(x)=R''(x)/R(x)$ remain stationary. With the boundary condition

$$\psi(0,t)=\cos(\omega t) \tag{6.2a}$$

reflecting a sinusoidal perturbation at $x=0$, one obtains from (4.17) in the long-time limit a purely periodic response for $\psi(x,t)=R(x)\phi(x,t)$ with the forcing frequency ω:

$$\begin{aligned}\psi(x,t)&=\hat{\psi}(x)\exp(i\omega t)+\text{c.c.}\\&=2|\hat{\psi}(x)|\cos[\omega t+\chi(x)] .\end{aligned} \tag{6.2b}$$

The complex oscillation amplitude $\hat{\psi}(x)=|\hat{\psi}(x)|e^{i\chi(x)}$ obeys the equation

$$\left[i\frac{\omega}{D_0}-\partial_x^2+V(x)\right]\hat{\psi}(x)=0 , \tag{6.2c}$$

with the boundary conditions

$$\hat{\psi}(0)=\tfrac{1}{2},\quad \hat{\psi}(L)=0 . \tag{6.2d}$$

1. *Two test problems*

To get a feeling for the effect of a spatially varying modulus $R(x)$ of the pattern under periodic perturbation, we consider first profiles like the test problems (3.9a) and (3.10a) treated in Sec. III A 2. For these modulus profiles the potential is constant, $V(x)=\bar{V}$, and the solution of (6.2c) is

$$\hat{\psi}(x)=\tfrac{1}{2}\frac{\sinh[\bar{\mathcal{K}}(L-x)]}{\sinh(\bar{\mathcal{K}}L)} . \tag{6.3a}$$

The characteristic exponent

$$\bar{\mathcal{K}}=\sqrt{\bar{V}+i\omega/D_0} \tag{6.3b}$$

is complex with real and imaginary parts:

$$\bar{\mathcal{K}}_r=\left[\frac{|\bar{\mathcal{K}}|^2+\bar{V}}{2}\right]^{1/2},\quad \bar{\mathcal{K}}_i=\left[\frac{|\bar{\mathcal{K}}|^2-\bar{V}}{2}\right]^{1/2} , \tag{6.3c}$$

and

$$|\bar{\mathcal{K}}|^2=\sqrt{\bar{V}^2+\omega^2/D_0^2} . \tag{6.3d}$$

The solution (6.3) most clearly reveals (i) finite size effects and (ii) the effect of an amplitude variation of the pattern

represented by a nonzero $V(x)$.

Consider first the effect (i): Only for $e^{2\bar{\mathcal{K}}_r(L-x)} \gg 1$ is the solution [(6.2b) and (6.3)] a damped phase wave:

$$\psi(x,t) \simeq \text{const} \times e^{-\bar{\mathcal{K}}_r x} \cos(\omega t - \bar{\mathcal{K}}_i x) , \tag{6.4}$$

with an x-independent spatial decay rate $\bar{\mathcal{K}}_r$ and an x-independent wave number $\bar{\mathcal{K}}_i$. Otherwise, the decay rate of $|\hat{\psi}(x)|$ as well as the wave number $-\partial_x \chi(x)$ are not constant.

(ii) Only when amplitude variations are ignored by setting $\bar{V}=0$, i.e., only in the limit of the simple diffusion equation, is $\bar{\mathcal{K}}_r = \bar{\mathcal{K}}_i = \mathcal{K}_0 = \sqrt{\omega/2D_0}$. Yet, with

$$\hat{\psi}(x) = \frac{1}{2} \frac{\sinh[(1+i)\mathcal{K}_0(L-x)]}{\sinh[(1+i)\mathcal{K}_0 L]} , \tag{6.5}$$

the wave number and the decay rate still vary with x if $\mathcal{K}_0(L-x)$ is not large enough. A nonvanishing potential $\bar{V}$, on the other hand, causes $\bar{\mathcal{K}}_r$ to be different from $\bar{\mathcal{K}}_i$. In particular, for the convex text profile

$$R(x) = e^{-x/l} + e^{-(L-x)/l}$$

(3.9a) that looks somewhat similar to that of TVF, one has $\bar{V} = 1/l^2$. Then the decay rate $\bar{\mathcal{K}}_r$ is larger than the wave number $\bar{\mathcal{K}}_i$. However, for the concave test profile

$$R(x) = \cos[\beta\pi(x - L/2)/L]$$

(3.10a) which shows some similarity to RBC, one has $\bar{V} = -\beta^2\pi^2/L^2$, and consequently $\bar{\mathcal{K}}_r < \bar{\mathcal{K}}_i$. These examples show the main features that can be seen also for space-dependent potentials $V(x) = R''(x)/R(x)$: a locally convex modulus tends to decrease the local wave number of the phase wave and to increase the decay rate and vice versa for a locally concave $R(x)$.

2. *Phase waves under the JEF modulus of the GLE*

We now investigate RBC with the potential (4.9) that is given in terms of a JEF following from the solution of the GLE. Then Eq. (6.2c) takes the form of a Lamé equation [37,43]:

$$\left[\partial_y^2 - 2m\, \mathrm{sn}^2(y|m) - m - 1 + \frac{i}{2} \left[\frac{\mathcal{K}_0 L}{K(m)} \right]^2 \right] \hat{\psi}(y) = 0 , \tag{6.6a}$$

$$y = 2K(m)x/L . \tag{6.6b}$$

Its two fundamental solutions are

$$\hat{\psi}_{1,2}(y) = \frac{H(y \mp y^*|m)}{\Theta(y|m)} \exp[\pm y Z(y^*|m)] , \tag{6.7a}$$

where y^* is the characteristic root of

$$\mathrm{dn}^2(y|m) = -(2m+1) - \frac{i}{2} \left[\frac{\mathcal{K}_0 L}{K(m)} \right]^2 . \tag{6.7b}$$

Here, H, Θ, and Z are elliptic functions [42]. The solution (6.7a) is nearly a complex exponential function distorted by the additional elliptic functions, which represent the influence of the boundary condition on the phase wave. Since

$$H(y|m)/\Theta(y|m) = \mathrm{sn}(y|m) ,$$

this prefactor has a shape similar to that of the modulus function $R(x)$.

B. Comparison with experiments

1. *Rayleigh-Bénard convection*

First we discuss and compare with the very carefully performed experiments of Wesfreid and Croquette [16]. They extracted in a RB system of length $L = 30d$ the wave number of the observed phase wave from a linear best fit to its phase shift. The decay rate was obtained by fitting the magnitude of the phase perturbation to a simple exponential function. Both fits were done in a range between $2d$ and $8d$ away from the source of the perturbation. The wave source was in the middle of their cell. These experimental quantities thus have to be compared with the imaginary and real parts of the logarithmic derivative

$$\mathcal{K}(x) = -\partial_x \ln \hat{\psi}(x) = -\partial_x \ln|\hat{\psi}(x)| - i\partial_x \chi(x) \tag{6.8}$$

of the complex amplitude $\hat{\psi} = |\hat{\psi}| e^{i\chi}$ that solves (6.2). The real part $\mathcal{K}_r = -\partial_x \ln|\hat{\psi}|$ is the local decay rate of the modulus and the imaginary part $\mathcal{K}_i = -\partial_x \chi$ is the local wave number of the phase wave (6.2b). Note that $\mathcal{K}_r(x)$ and $\mathcal{K}_i(x)$ approach $\mathcal{K}_0$ for a pure diffusion equation in a very long system, e.g., for $V \equiv 0$ one finds from (6.5)

$$\mathcal{K}(x) = (1+i)\mathcal{K}_0 \coth[(1+i)\mathcal{K}_0(L-x)] , \tag{6.9}$$

so that $\mathcal{K}$ equals $(1+i)\mathcal{K}_0$ plus exponential corrections of size $\exp[-2\mathcal{K}_0(L-x)]$ for large $\mathcal{K}_0(L-x)$. However, for the experimental setup [16] these two idealizations do not really apply: (i) The rigid sidewall is only $15d$ away from the source so that the effective length of the system is reduced to $L_{\text{eff}} = 15d$, and (ii) for the container length $L = 30d$ the parameter $\alpha = 31.16$ is small so that the sidewall-induced variations of the convection amplitude require going beyond the simple diffusion equation $V \equiv 0$ and incorporating $V(x)$ properly in (6.2c) or in the Lamé equation (6.6).

In Fig. 11 we show for two modulation frequencies $\omega = 0.15\kappa/d^2$ (top row) and $0.66(\kappa/d^2)$ (bottom row), the real part (solid lines) and the imaginary part (dashed lines) of $\mathcal{K}(x)$ (6.9) for the solution (6.5) of the idealized diffusion equation, $V(x) \equiv 0$, in comparison with $\mathcal{K}(x)$ resulting from the Lamé equation (6.6) with the sidewall-induced potential $V(x)$ given in terms of the JEF for $R(x)$. Here x is the distance from the wave source where the periodic phase perturbation is enforced. To compare with [16], we have used in Eq. (6.9) the effective propagation length $L_{\text{eff}} = 15d$ available for phase waves in that experiment with total length $L = 30d$, $\epsilon = 0.16$, $\alpha = 31.2$, $\mathrm{Pr} = 492$, and $D_0 = 2.92\kappa$. For the smaller frequency, $\mathcal{K}_0 L_{\text{eff}} = 2.4$ is so small that differences between $\mathcal{K}_r$ and $\mathcal{K}_i$ resulting from the diffusion equation are visible al-

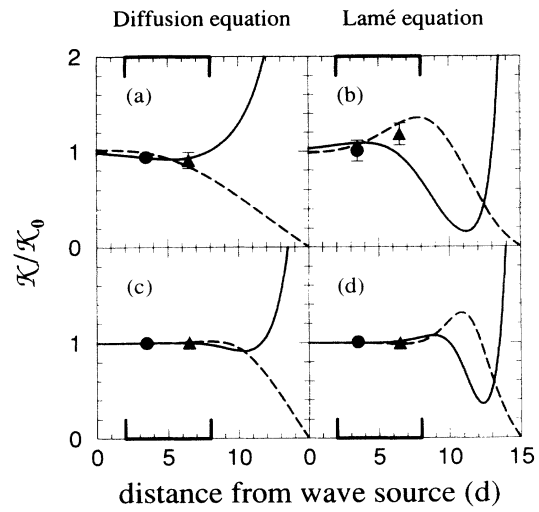

FIG. 11. Local decay rates $\mathcal{K}_r(x)$ (solid lines) and wave numbers $\mathcal{K}_i(x)$ (dashed lines) of damped phase waves generated by periodic perturbations of frequency $\omega=0.15\kappa/d^2$ [(a) and (b)] and $\omega=0.66\kappa/d^2$ [(c) and (d)] versus distance x from the source. In the Lamé equation (6.6), sidewall-induced variations of the convective amplitude $R(x)$ are incorporated via the potential $V(x)$. In the diffusion equation $V\equiv 0$, they are not. The symbols with vertical bars are spatial averages and standard variations of $\mathcal{K}_r$ (circles) and $\mathcal{K}_i$ (triangles) over the interval indicated by thick braces. We used the parameters $\epsilon=0.16$, $\alpha=31.2$, Pr=492, $D_0=2.92\kappa$, $L=30d$, and $L_{\text{eff}}=L/2$ of the experiment [16]. See the text for further details.

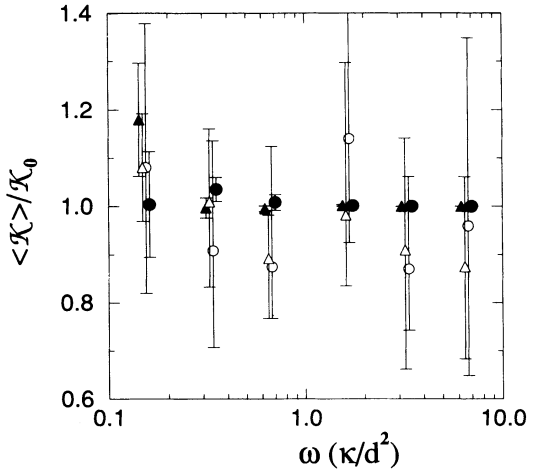

FIG. 12. Spatial averages of the local amplitude decay rate $\langle\mathcal{K}_r(x)\rangle$ (circles) and of the local wave number $\langle\mathcal{K}_i(x)\rangle$ (triangles) of phase waves versus the logarithm of the frequency. The open symbols come from experiments [16] and the solid symbols from the Lamé equation (6.6) where sidewall-induced variations of the convective amplitude $R(x)$ are incorporated via the potential $V(x)$. The parameters for the experiment and the Lamé equation are the same (cf. Fig. 11). The spatial average is taken over an interval $(2d,8d)$ away from the wave source, as indicated in Fig. 11. The vertical bars are standard deviations.

ready in the range $2d<x<8d$ marked by thick braces in Fig. 11 where the experimental data were fitted. For the larger frequency, $\mathcal{K}_0L_{\text{eff}}=5.0$. The differences are too small to be seen in the fit range. The spatial averages $\langle\mathcal{K}(x)\rangle$ over the interval $(2d,8d)$, i.e., the quantities that one would obtain with the employed fit procedure, are shown by solid symbols (circles for $\langle\mathcal{K}_r\rangle$ and triangles for $\langle\mathcal{K}_i\rangle$) together with their standard variations (vertical bars). Since, with increasing distance from the wave source, $\mathcal{K}_r(\mathcal{K}_i)$ rapidly approaches $+\infty(0)$, at the end, $x=L_{\text{eff}}$, of the system, the fitted values sensitively depend on the choice of the fit interval if $\mathcal{K}_0L_{\text{eff}}$ is too small.

Comparing the result of the diffusion equation with the Lamé equation, one sees that incorporating the variation of $R(x)$ in the latter causes a stronger variation of $\mathcal{K}(x)$ with additional extrema: close to (further away from) the wave source, $\mathcal{K}_r$ is shifted upwards (downwards) and vice versa for $\mathcal{K}_i$. Both are a consequence of the term $H(y\mp y^*)/\Theta(y)$ in formula (6.7a). The characteristic root y^* breaks the midline symmetry at $x=L/2$ of the JEF $\text{sn}(y)=H(y)/\Theta(y)$. Thus, the simplified argument with the concave test profile (3.10a) which yields $\mathcal{K}_r<\mathcal{K}_i$ is not valid there. However, the spatial averages over the marked region fulfill such a relation by accident for the smaller frequency.

In Fig. 12 we have plotted the averaged decay rates $\langle\mathcal{K}_r\rangle$ (circles) and wave numbers $\langle\mathcal{K}_i\rangle$ (triangles) from the Lamé solution (solid symbols) for different frequencies in comparison with the result of [16] (open symbols). Taking into account the large error bars of the experiment, it is impossible to decide whether the spatially averaged data are better represented by the Lamé equation (6.6) or the diffusion equation (2.1).

2. *Taylor vortex flow*

We also applied Eq. (6.2) to the TVF case. Since we do not know a closed analytic solution as in RBC, we solved Eq. (6.2c) numerically. For the parameters $\eta=0.882$, $L=70.4d$, $\epsilon=0.074$, $\alpha=70.9$, and $\omega=2.54\times10^{-2}\nu/d^2$ of Wu and Andereck [20], we integrated Eq. (6.2c) with $V(x)$ calculated from an envelope $R(x)$ of the axial velocity component of the solution of our full 2D NSE. As in RBC, we find in the region where the experimental data are taken, a phase wave with $\mathcal{K}_r(x)\simeq\mathcal{K}_0$ and $\mathcal{K}_i(x)\simeq\mathcal{K}_0$. So we do not find the experimentally observed relatively strong splitting of $\mathcal{K}_r$ and $\mathcal{K}_i$ away from $\mathcal{K}_0$, as shown in Fig. 6 of the second article in Ref. [20].

3. *Forced phase waves versus phase diffusion*

At the end of this section we want to stress that the dynamical properties of damped phase waves emitted by periodically applied forces are in general—if the governing equation for the phase is not an ideal diffusion equation—unrelated to and different from the free diffusive relaxation of an initially prepared perturbation. A periodic phase perturbation generates a damped phase

wave with spatially varying local decay rates $\mathcal{K}_r(x)$ and local wave numbers $\mathcal{K}_i(x)$. In the chosen experimental measurement ranges [16,20], both quantities happened to be close to the value $\mathcal{K}_0$ resulting from a Stokes layer. It should be noted, however, that (i) both these quantities vary with distance x from the wave source in a way that depends on the experimental parameters and (ii) $\mathcal{K}_r$ and $\mathcal{K}_i$ are in general unrelated to the free diffusive relaxational behavior of an initially prepared phase perturbation that is characterized by an effective diffusion constant D.

VII. CONCLUSION

We have studied how phase dynamics is influenced by lateral boundaries in dissipative nonequilibrium pattern forming systems like Rayleigh-Bénard convection or Taylor vortex flow. To that end, we used a generalized phase diffusion equation and numerical simulations of the full 2D field equations. The ordinary phase diffusion equation originally derived by Pomeau and Manneville [3] does not contain finite size effects. The experiment of Gerdts [19], however, reveals deviations from theoretical expectations which are connected to the boundaries of the Taylor-Couette setup. We have incorporated such effects into a phase description in the following way: Starting from the Ginzburg-Landau amplitude equation, an expansion around the final stationary state is performed. The modulus and phase deviations from the final state evolve on distinct time scales provided the combination $\alpha=\epsilon^{1/2}L/\xi_0$ of relative control parameter ϵ and system length L scaled by the coherence length ξ_0 is large. This is typically fulfilled in experiments. If, in addition, the wave number of the final pattern is close to the critical one, then we end up with a phase equation containing the space derivative of the envelope profile $R(x)$. Exactly that is the point where the phase dynamics is changed by the lateral ends because they lead to spatial nonuniformities in $R(x)$. In RBC, sidewalls suppress convection, so $R(x)$ bends downwards. On the other hand, for TVF, boundary-induced Ekman vortices enhance the envelope profile. We have employed our generalized phase diffusion equation to investigate two different problems that have also been addressed in experiments: the free decay of initially applied perturbations [17,19,20] and the response to periodic forcing [16,20].

(a) Decay of an initially applied perturbation. The system relaxes in a diffusive manner and the decay rates of the different modes can be related to the eigenvalues of the phase equation. The slowest mode surviving in the long-time limit gives rise to the definition of an "effective" diffusion constant D/D_0 as the smallest positive eigenvalue. We found it advantageous to transform the eigenvalue problem of the phase equation into a stationary Schrödinger equation where the modulus enters via a potential

$$V(x)=[\partial_x^2 R(x)]/R(x) .$$

The envelope profile $R(x)$ is taken from the stationary GLE yielding Jacobian elliptic functions as solutions or from the final state of numerical simulations of the full field equations. Using the GLE moduli, we found the following.

(i) The eigenvalues of the Schrödinger problem and with it the effective diffusion constant D/D_0 are functions of only one parameter, namely, α.

(ii) In both systems, RBC and TVF, D/D_0 is significantly higher (up to a factor of 3) as it would be for an ideal reference system with $R=$const.

(iii) For RBC, the GLE Schrödinger problem contains a zero eigenvalue that allows an undamped shift of the pattern as a whole.

(iv) Beyond the zero eigenvalue, the spectra of RBC and TVF are identical because their corresponding potentials coming from the GLE are connected by a commutation relation similar to one appearing in supersymmetric quantum mechanics.

(v) In TVF, the data of Gerdts's experiment [19] as well of our own numerical simulations of the full 2D Navier-Stokes equations confirm the theoretical predictions. Slight deviations can be explained by the fact that the amplitude equation itself does not describe TVF well enough for higher ϵ due to the inflow-outflow asymmetry [22].

(vi) For RBC, our numerical simulations show a long lasting nondiffusive, almost global, movement of the pattern. We relate this behavior of the full system of equations to the zero eigenvalue in the phase equation that allows a free translational mode. The full hydrodynamic field equations, however, provide some mechanism responsible for the initial start of such motion and its eventual slowing down which is contained neither in the amplitude equation nor in the phase equation derived from it.

(vii) After subtraction of the behavior in (vi), one can extract diffusive modes fitting well to the predicted values. On the other side, the experimental results of Croquette and Schosseler [17] seem to be more related to the zero eigenvalue dynamics. This might explain that the measured relaxations lie about 30% below the theoretical values.

(b) Response to time-periodic forcing. In a long system, spatially localized periodic forcing generates a damped phase wave propagating away from the source. The properties of the phase wave can be characterized by two independent quantities: a local wave number $\mathcal{K}_i(x)$ and a local decay rate $\mathcal{K}_r(x)$. In the case of a simple phase diffusion equation (2.1) and for a semi-infinite system, both quantities have the same value and are connected with the diffusion constant D_0 via the inverse width of the Stokes layer, $\mathcal{K}_0=\sqrt{\omega/2D_0}$. In general, $\mathcal{K}_r$ and $\mathcal{K}_i$ differ from $\mathcal{K}_0$ for two reasons. If the system is not long enough, the second fundamental solution of the pure phase diffusion equation for a phase wave propagating inwards cannot be discarded. It causes $\mathcal{K}_i(x)$ and $\mathcal{K}_r(x)$ to deviate substantially from $\mathcal{K}_0$ when the frequency is small as, e.g., for the smallest frequencies in Ref. [16]. In addition, the boundary-induced amplitude variation influences the damped phase wave. As in (*a*), the effect enters via a potential term in a Schrödinger-like equation. Hence, we get the following results.

(i) For simple amplitude profiles leading to $V(x)=\text{const}$ (Sec. III A 2) $\mathcal{K}_r(x)$ and $\mathcal{K}_i(x)$ are constant. But the values split up from $\mathcal{K}_0$ according to the sign of V, e.g., $V>0$ implies $\mathcal{K}_r>\mathcal{K}_i$. Already for this case the Stokes layer relations between wave number, decay rate, and diffusion constant are destroyed.

(ii) For RBC, a closed solution for the phase equation with amplitude profiles $R(x)$ taken from the GLE can be given. Because of the finiteness of the system and of amplitude variations, the resulting wave numbers $\mathcal{K}_i(x)$ and decay rates $\mathcal{K}_r(x)$ are space dependent in a way that changes with ω, L, and ϵ. In general, in finite systems the characteristic properties of periodically forced phase waves are unrelated to the diffusive behavior after an initial phase perturbation.

ACKNOWLEDGMENTS

We thank H. Riecke for providing his results of the calculation of the diffusion constant in TVF and J. von Stamm and G. Pfister, who sent us the original data of the unpublished experiment done by U. Gerdts. This work was supported by the Stiftung Volkswagenwerk.

[1] H. Brand, in *Pattern, Defects and Material Instabilities,* Vol. 183 of *NATO Advanced Study Institute, Series B: Physics,* edited by D. Walgraef and N. M. Ghoniem (Kluwer, Dordrecht, 1990), p. 25; Y. Kuramoto, *Chemical Oscillations, Waves, and Turbulence* (Springer, Berlin, 1984).

[2] M. C. Cross and P. C. Hohenberg, Rev. Mod. Phys. **65**, 851 (1993).

[3] Y. Pomeau and P. Manneville, J. Phys. (Paris) Lett. **40**, L609 (1979).

[4] M. C. Cross, Phys. Rev. A **27**, 490 (1983); P. Manneville and J. M. Piquemal, *ibid.* **28**, 1774 (1983).

[5] A. Zippelius and E. D. Siggia, Phys. Fluids **26**, 2905 (1983); L. Kramer and W. Zimmermann, Physica D **16**, 221 (1985).

[6] H. Riecke and H.-G. Paap, Phys. Rev. Lett. **59**, 2570 (1987); L. Ning, G. Ahlers, and D. S. Cannell, *ibid.* **64**, 1235 (1990); I. Rehberg, E. Bodenschatz, B. Winkler, and F. H. Busse, *ibid.* **59**, 282 (1987).

[7] H.-G. Paap and H. Riecke, Phys. Fluids A **3**, 1519 (1991); H. Riecke (private communication).

[8] P. Coullet and G. Iooss, Phys. Rev. Lett. **64**, 866 (1990).

[9] M. C. Cross and A. C. Newell, Physica D **10**, 229 (1984); A. C. Newell, Th. Passot, and M. Souli, J. Fluid Mech. **220**, 187 (1990).

[10] Y. Pomeau and P. Manneville, J. Phys. (Paris) **42**, 1067 (1981); Y. Pomeau and S. Zaleski, J. Phys. (Paris) Lett. **44**, L135 (1983).

[11] L. Kramer, E. Ben-Jacob, H. Brand, and M. C. Cross, Phys. Rev. Lett. **49**, 1891 (1982).

[12] V. Croquette and A. Pocheau, in *Cellular Structures in Instabilities,* edited by J. E. Wesfreid and S. Zaleski, Lecture Notes in Physics Vol. 210 (Springer, Berlin, 1984), p. 104; V. Steinberg, G. Ahlers, and D. S. Cannell, Phys. Scr. **32**, 534 (1985).

[13] L. Kramer and H. Riecke, Z. Phys. B **59**, 245 (1985); J. C. Buell and I. Catton, Phys. Fluids **29**, 23 (1986); J. Fluid Mech. **171**, 477 (1986); H. Riecke, Europhys. Lett. **2**, 1 (1986); Phys. Rev. A **37**, 636 (1988); M. A. Dominguez-Lerma, D. S. Cannell, and G. Ahlers, *ibid.* **34**, 4956 (1986).

[14] E. D. Siggia and A. Zippelius, Phys. Rev. A **24**, 1036 (1981); Y. Pomeau, S. Zaleski, and P. Manneville, *ibid.* **27**, 2710 (1983); A. Pocheau and V. Croquette, J. Phys. (Paris) **45**, 35 (1984).

[15] P. Coullet, L. Gil, and J. Lega, Phys. Rev. Lett. **62**, 1619 (1989); Physica D **37**, 91 (1989); H. Chaté and P. Manneville, Phys. Rev. Lett. **58**, 112 (1986); J. J. Hegseth, C. D. Andereck, F. Hayot, and Y. Pomeau, *ibid.* **62**, 257 (1989).

[16] J. E. Wesfreid and V. Croquette, Phys. Rev. Lett. **45**, 634 (1980).

[17] V. Croquette and F. Schosseler, J. Phys. (Paris) **43**, 1183 (1982).

[18] A. Pocheau, V. Croquette, P. Le Gal, and C. Poitou, Europhys. Lett. **3**, 915 (1987).

[19] U. Gerdts, Ph.D. thesis, Kiel University, 1985; J. von Stamm and G. Pfister (private communication).

[20] M. Wu and C. D. Andereck, Phys. Rev. A **43**, 2074 (1991); Phys. Fluids A **4**, 2432 (1992).

[21] P. Tabeling, J. Phys. (Paris) Lett. **44**, L665 (1983).

[22] M. Lücke and D. Roth, Z. Phys. B **78**, 147 (1990).

[23] M. C. Cross, Phys. Fluids **23**, 1727 (1980).

[24] M. A. Dominguez-Lerma, G. Ahlers, and D. S. Cannell, Phys. Fluids **27**, 856 (1984).

[25] R. Graham and J. A. Domaradzki, Phys. Rev. A **26**, 1572 (1982).

[26] R. P. Behringer and G. Ahlers, Phys. Lett. **62A**, 329 (1977).

[27] J. Wesfreid, Y. Pomeau, M. Dubois, C. Normand, and P. Bergé, J. Phys. (Paris) Lett. **39**, L725 (1978); J. Wesfreid, P. Bergé, and M. Dubois, Phys. Rev. A **19**, 1231 (1979).

[28] J. Niederländer, M. Lücke, and M. Kamps, Z. Phys. B **82**, 135 (1991).

[29] G. Pfister and I. Rehberg, Phys. Lett. **83A**, 19 (1981).

[30] J. P. Gollub and M. H. Freilich, Phys. Fluids **19**, 618 (1976); G. Ahlers, D. S. Cannell, M. A. Dominguez-Lerma, and R. Heinrichs, Physica D **23**, 202 (1986); R. Heinrichs, D. S. Cannell, G. Ahlers, and M. Jefferson, Phys. Fluids **31**, 250 (1988).

[31] A. C. Newell and J. A. Whitehead, J. Fluid Mech. **38**, 279 (1969).

[32] L. A. Segel, J. Fluid Mech. **38**, 203 (1969).

[33] The relation of α to other combinations of ϵ and L appearing in a different context in the literature is $\alpha=2\delta$ [34] and $\alpha^2=4\delta$ [35].

[34] M. C. Cross, P. G Daniels, P. C. Hohenberg, and E. D. Siggia, J. Fluid Mech. **127**, 155 (1983).

[35] P. G. Daniels, Proc. R. Soc. London, Ser. A **358**, 173 (1977); S. N. Brown and K. Stewartson, *ibid.* **360**, 455 (1978).

[36] M. Lücke, M. Mihelcic, and K. Wingerath, Phys. Rev. A **31**, 396 (1985).

[37] E. L. Ince, *Ordinary Differential Equations* (Dover, New York, 1956).

[38] L. Infeld and T. E. Hull, Rev. Mod. Phys. **23**, 21 (1951).

[39] M. M. Crum, Q. J. Math. Oxford **6**, 121 (1955); P.A. Deift, Duke Math. J. **45**, 267 (1978).

[40] C. W. Hirt, B. D. Nichols, and N. C. Romero, Los Alamos Scientific Laboratory Report No. LA-5652, 1975 (unpublished).

[41] E. L. Ince, Proc. R. Soc. Edinburg **60**, 47 (1940); **60**, 83 (1940).

[42] *Handbook of Mathematical Functions,* edited by M. Abramowicz and I. Stegun (Dover, New York, 1965).

[43] E. T. Whittaker and G. N. Watson, *A Course of Modern Analysis* (Cambridge University, London, 1969).